RSC Advances

PAPER

View Article Online
View Journal | View Issue

Cite this: *RSC Adv.*, 2025, **15**, 41546

# A highly accurate and selective non-enzymatic glucose sensor based on a $Fe_2O_3/CuFe_2O_4$/graphene nanoplatelet nanocomposite

Lilia Bourouba, *[abc] Emna Zouaoui,[cd] Messaoud Benounis,[b] Hend S. Magar *[e] and Abdecharif Boumaza[f]

Received 7th October 2025
Accepted 21st October 2025

DOI: 10.1039/d5ra07666h

rsc.li/rsc-advances

In this study, a sensitive and accurate non-enzymatic glucose sensor based on a $Fe_2O_3/CuFe_2O_4$/graphene nanoplatelet (GNPs) nanocomposite was performed. The nanocomposite was synthesized *via* a facile hydrothermal method and characterized using FTIR, XRD, SEM, Raman, XPS, cyclic voltammetry (CV) and electrochemical impedance spectroscopy techniques. The integration of $Fe_2O_3$ and $CuFe_2O_4$ with graphene nanoplatelets (GNPs) provides a synergistic effect, enhanced surface area, high electrochemical conductivity and improved catalytic activity toward glucose oxidation. Electrochemical measurements using CV and chronoamperometry demonstrated excellent sensing performance, with high sensitivity of 62.4 μA $mM^{-1}$ $cm^{-2}$, a lower of detection limit of 0.049 μM (S/N = 3) and a widely linear detection range from 5–75 μM and 75–13 000 μM. The sensor exhibited outstanding selectivity against common interfering species (*e.g.*, dopamine, uric acid and ascorbic acid), along with good stability and reproducibility. These findings suggest that the $Fe_2O_3/CuFe_2O_4$/GNPs nanocomposite is a promising applicant for glucose non-enzymatic sensing in clinical and biomedical applications.

## 1. Introduction

Glucose monitoring has a critical role in the management of diabetes mellitus, a chronic metabolic disorder affecting millions worldwide. Accurate and reliable glucose levels detection is essential for diagnosis and daily glucose control. Among various glucose sensing technologies, electrochemical sensing[63,65,73,77] has gained significant consideration due to its rapid response,[66,67] ease of operation,[39,68] high sensitivity[62,67] and low cost.[61,64] Traditionally, enzymatic glucose sensors based on glucose oxidase (GOx) have dominated the market. However, these sensors suffer from several limitations, including poor stability, high production cost, and susceptibility to different conditions such as pH, temperature, and humidity.[64] In recent years, non-enzymatic electrochemical glucose sensors have emerged as promising alternatives. These sensors depend on direct glucose oxidation on the surface of the electrode, offering enhanced stability and reproducibility without the need for biological components. The performance of such sensors is dependent on the electrocatalytic properties of the electrode materials.

Transition metal oxides and spinel ferrites have attracted significant interest due to their brilliant redox activity,[27,69] chemical stability,[70] and catalytic potential.[71,72] Among them, $Fe_2O_3$ and $CuFe_2O_4$ are particularly appealing owing to their abundance, environmental friendliness, and strong catalytic behavior toward glucose oxidation. However, their inherent low electrical conductivity limits their standalone performance. To address this challenge, incorporating conductive carbon-based materials such as graphene can significantly enhance electron transport and increase active surface area. $CuFe_2O_4$, a transition metal oxide, has garnered significant attention as an electrocatalyst in the development of electrochemical sensors, particularly for non-enzymatic glucose detection, owing to its excellent structural tunability, electrocatalytic activity, and compatibility with a wide range of nanocomposite configurations. $CuFe_2O_4$ employed in sensing other biomolecules. For example, Atacan [5] developed a glassy carbon electrode modified with a $CuFe_2O_4$/rGO decorated with gold nanoparticles, which approved a good sensitivity and a broad linear range for detecting L-cysteine hematite (α-$Fe_2O_3$) is extensively utilized in sensor development due to its favorable semiconducting

---

[a] Research Laboratory on Physical Chemistry of Surfaces and Interfaces (LRPCSI), Department of Process Engineering, Faculty of Technology, University of 20 August 1955, Skikda 21000, Algeria. E-mail: hendamer2000@yahoo.com; l.bourouba@univ-skikda.dz

[b] Laboratory of Sensors, Instrumentation and Processes (LCIP), University of Abbess Laghrour, Khenchela 40000, Algeria

[c] Laboratory of Catalysis, Bioprocess and Environment, Faculty of Technology, (LCBE) University of 20 August 1955, Skikda 21000, Algeria

[d] Laboratory for the Application of Chemistry to Natural Resources and Substances and the Environment (LACReSNE), Faculty of Sciences, Bizert, Tunisia

[e] Applied Organic Chemistry Department, National Research Centre, Dokki, P.O. Box.12622 Giza, Egypt

[f] Laboratory of Structures, Properties and Interatomic Interactions (LASPI²A), Abbes Laghrour University, Khenchela 40000, Algeria

characteristics, excellent chemical stability, and notable catalytic activity. Its natural abundance and environmental friendliness further enhance its suitability, particularly for applications in medical diagnostics and environmental monitoring.[108] In non-enzymatic glucose detection, $Fe_2O_3$ offers a stable, low-toxicity alternative to enzyme-based sensors. Nanostructures like porous nanorods and nanoparticles, particularly when combined with materials such as rGO or g-$C_3N_4$, enhance performance by increasing surface area and improving electron transfer. These composites allow for sensitive glucose detection at physiological pH, even in complex samples.[41,106,115] Electrochemical methods like CV and DPV are used to fine-tune these sensors, supporting their potential for real-world, portable applications.[18,94] Meanwhile, graphene nanoplatelets (GNPs) have emerged as key electrode modifiers in sensor for glucose detection, primarily due to their highly surface area and excellent electron transport properties. These features significantly improve glucose adsorption and electrocatalytic oxidation efficiency.[28,49,89] π–π interactions between glucose molecules and GNPs enhance molecular adsorption at the electrode surface, leading to lower detection limits and improved sensitivity.[89] Graphene-based nanocomposites offer several advantages for enzyme-free glucose detection in alkaline media, driven by graphene's exceptional electrical conductivity and physicochemical stability.[55] Strategic incorporation of graphene with metal oxides or other conductive nanomaterials can further amplify sensor performance. Notable examples include graphene–CuO, graphene sheet/graphene nanoribbon/nickel nanoparticles (GS/GNR/Ni), and graphene–ZnO–$SnO_2$ nanocomposites, all of which leverage synergistic effects to boost electrocatalytic activity and electron transfer rates.[31,47,48] Furthermore, graphene derivatives like GNPs are known to enhance sensor responsiveness by promoting fast electron mobility and efficient glucose molecule adsorption, thus significantly improving detection thresholds and response times.[10,22] This study highlights the potential of $Fe_2O_3/CuFe_2O_4$/GNPs nanocomposites as efficient and reliable electrode materials for non-enzymatic glucose sensing applications. The synergistic interaction between $Fe_2O_3$ and $CuFe_2O_4$, combined with the exceptional conductivity and large surface area of GNPs, results in a highly sensitive and stable electrode material. The nanocomposite was synthesized *via* a simple hydrothermal route and thoroughly characterized using structural and electrochemical techniques. The resulting sensor exhibits excellent electrocatalytic performance, with brilliant sensitivity, lower detection limit, widely linear range and good selectivity against common interfering species.

## 2. Experimental

### 2.1. Materials and methods

Monohydrate of α-D-lactose (Lac), D-(+)-mannose (Man), D-(+)-galactose (Gal) and D-(+)-glucose were brought from Fluka (USA). Fructose, maltose, sucrose, urea, uric acid (UA), L-ascorbic acid (AA) were obtained from Sigma (USA). Monopotassium phosphate ($KH_2PO_4$), sodium citrate ($Na_3C_6H_5O_7\cdot 2H_2O$), sodium chloride (NaCl), sodium hydroxide (NaOH), copper(II) chloride dihydrate, potassium permanganate ($KMnO_4$) (Panreac), potassium ferricyanide ($K_3[Fe\ (CN)_6]$), $FeCl_3$, ($CuCl_2\cdot 2H_2O$), and potassium ferrocyanide ($K_4[Fe(CN)_6]\cdot 3H_2O$), graphite powder 20 < μm were obtained from Sigma Aldrich. Graphene nanoplatelets 5 microns wide × 6–8 nm thick × was purchased Strem chemicals.

### 2.2. Apparatus and instrumentation

Fourier-transform infrared spectroscopy (FTIR) using a PerkinElmer instrument with a range of 4000–400 $cm^{-1}$ used for the structure and composition characterization of the samples. X-ray diffraction (XRD) analysis was produced using an XPERT diffractometer with Cu Kα radiation ($\lambda = 0.15450$ nm) to identify the crystalline phases presented in the nanocomposites fabrication. To analyze the microstructure and surface morphology of the nanocomposite, a Thermo Scientific Prisma E Scanning Electron Microscope (SEM) was used, operating at an accelerating voltage of 10 kV. The SEM was coupled with an energy-dispersive X-ray spectroscopy (EDS) detector to enable elemental analysis, X-ray photoelectron spectroscopy (XPS) JEOL, modèl JPS-9030 was employed to investigate the surface composition and oxidation states of the sample. The wide-scan spectra were collected using an Mg Kα radiation source (1253.6 eV) with a step size of 1.0 eV and a pass energy of 50 eV, covering a binding energy range of (0–1000) eV to identify the elemental composition of the samples. Raman spectroscopy measurements for the nanocomposite were conducted at room temperature using Raman Spectroscopy (Confocal Raman microscope, WITech, alpha-300R, excitation laser 532 nm and Laser power 1 mW) for the nanomaterials characterizations. Each spectrum was recorded in the range of 100–4000 $cm^{-1}$ and the sample was examined under multiple magnifications to capture detailed structural information. Electrochemical data were obtained from a Biologic EcLab Sp-300 potentiostat at the Laboratory of Sensors, Instrumentation, and Processes (LCIP), Khenchela University, with a three-electrode cell configuration. Reference electrode (Ag/AgCl electrode), Counter electrode (platinum electrode), and working electrode (the metal oxide modified paste electrode). The electrolyte solution was aqueous NaOH (0.5 M). Electrochemical impedance spectroscopy (EIS), cyclic voltammetry (CV), and chronoamperometry (CP) techniques were conducted for measurements. All stock solutions of glucose were stored at 4 °C after preparation. For CV measurements the potential range was −0.8–1.0 V at scan rate of 50 mV $s^{-1}$.

### 2.3. Methods

**2.3.1. Synthesis of $Fe_2O_3/CuFe_2O_4$ nanocomposite.** The $Fe_2O_3/CuFe_2O_4$ nanocomposite was synthesized using a co-precipitation method. A mixed solution of iron chloride (0.4 M) and copper chloride (0.2 M) was prepared. Subsequently, sodium hydroxide solution (NaOH, 3 M) was added dropwise to the mixture at room temperature 2 hours under continuous magnetic stirring at 700 rpm. The pH of the solution was carefully monitored and adjusted until it reached a value between 11 and 12, as described by Kashif Ali, Ali Bahadur,[1] and Abdul Jabbar.[1] The resulting suspension was then heated to 80 °

C and maintained at this temperature for one hour to facilitate the reaction. Afterward, the mixture was allowed to cool naturally to room temperature (~25 °Cover ~1 hour). The obtained precipitate was thoroughly washed with deionized water, ethanol and centrifuged for 10 minutes (3000 rpm) to separate the solid product from the supernatant. Then, the isolated precipitate was dried overnight at 80 °C and annealed at 630 °C for 7 hours, following the procedure reported by Selima and Khairy.[90]

**2.3.2. Preparation of un/modified electrodes.** The unmodified carbon paste electrode (CPE) was prepared by mixing paraffin oil with graphene nanoplates (GNPs) and graphite powder in appropriate proportions.[16,100] For the modified electrodes, varying percentages of the desired modifier ($Fe_2O_3$/$CuFe_2O_4$) were incorporated into a mixture containing graphite powder, graphene, and paraffin oil. Each formulation was homogenized by grinding in a mortar for at least 20 minutes to ensure a uniform paste[16] and then packed into a plastic syringe with a copper wire inserted to provide electrical contact. The surface of the electrode was polished with parchment paper before electrochemical testing.

*2.3.2.1 Electrode composition optimization.* A series of modified carbon paste electrodes (CPEs) were prepared to investigate the effect of graphene nanoplatelets (GNPs) content on glucose sensing performance.[16,125] Bare graphite (Gt) paste served as the control (0% GNPs). Modified pastes were fabricated by incorporating GNPs at varying mass percentages relative to the total carbon content (graphite + GNPs). The tested GNPs loadings were: (0%, 5%, 10%, 15%, 20%, 25%, 30%, 35%, 40%, 45%, 50%, and 100%).[99]

*2.3.2.2 Preparation of $Fe_2O_3$/$CuFe_2O_4$-modified graphite/graphene electrodes.* To evaluate the effect of $Fe_2O_3$/$CuFe_2O_4$ loading on sensor performance, a series of modified carbon paste electrodes were prepared using a base matrix composed of graphite powder and graphene nanoplatelets (GNPs). The $Fe_2O_3$/$CuFe_2O_4$ nanocomposite was incorporated into this carbon matrix at varying mass percentages: 1%, 3%, 5%, 7%, 9%, and 10% (relative to the total mass of the carbon content). The surface of each electrode was polished with parchment paper prior to use. These electrodes were then tested for their electrochemical response to glucose oxidation.[33,114]

**2.3.3. Electrochemical characterization.** Electrochemical impedance spectroscopy (EIS) and Cyclic voltammetry (CV) were employed to study the electrochemical properties of both unmodified and modified electrodes.[100] All measurements were performed in an electrolyte solution containing 0.1 M potassium chloride (KCl) and 5 mM potassium ferrocyanide/ferricyanide $[Fe\ (CN)_6]^{3-/4-}$ as a redox probe.[11,100] CV measurements were produced within a potential range from −0.8 V to +1.0 V and a scan rate of 50 mV $s^{-1}$.[16,100] The EIS data were produced at open circuit potential (OCP) with a small AC perturbation amplitude of 5 mV, across a frequency range from 100 mHz to 100 kHz (ref. 100) The resulting Nyquist plots were analyzed using an appropriate equivalent circuit model to evaluate interfacial properties and charge-transfer resistance, providing insights into the electrode surface structure and conductivity.[33,100] Both unmodified and $Fe_2O_3$/$CuFe_2O_4$/GNPs-modified electrodes were characterized under identical conditions for comparative analysis.[33,100,114]

**2.3.4. Chronoamperometric analysis of non-enzymatic glucose sensing.** Chronoamperometric measurements were performed to evaluate the performance of the optimized carbon paste electrode modified with graphene nanoplatelets (GNPs) and $Fe_2O_3$/$CuFe_2O_4$ nanocomposite for non-enzymatic glucose detection.[33,56] The experimental conditions were systematically optimized, including the applied accumulation potential, analyte concentrations, and electrode composition.[24] A comprehensive interference study was also conducted to assess the selectivity of the sensor in the presence of common electroactive species.[46] Additionally, the sensor was applied to the quantitative analysis of glucose in real human serum samples.

**2.3.5. Chronoamperometric analysis of glucose in real serum samples.** The practical applicability of the developed sensor was validated by measuring glucose concentrations in human serum samples obtained from both diabetic and non-diabetic individuals.[11] For analysis, 100 μL of serum was mixed with 100 μL of glucose solution and diluted in 20 mL of 0.5 M sodium hydroxide.[125] Chronoamperometric measurements were carried out at a fixed applied potential of +0.6 V, and the current response was recorded over time.[24,56]

To evaluate the accuracy of the sensor, the standard addition method was employed by spiking known concentrations of glucose into the serum samples.[125] The recovery rates were calculated to assess precision and reliability.[11] The results obtained using the proposed sensor were compared with those from a commercial glucometer, demonstrating good agreement and confirming the sensor's potential for real-sample glucose monitoring.[11]

# 3. Results and discussion

## 3.1. Physical characterization

The FTIR analysis provides compelling evidence for the successful fabrication of the Gt,GNPs,Gt/GNPs and $Fe_2O_3$/$CuFe_2O_4$ /GNPs/Gt composite and its subsequent electrochemical activity towards glucose oxidation. The spectrum of the pristine electrode (the composite modified electrode before detection) confirms the composite's structure (see Fig. 1A), displaying characteristic bands of the carbon matrix (O–H at ~3450 $cm^{-1}$ and C=C at ~1630 $cm^{-1}$) alongside a distinct absorption band in the 500–700 $cm^{-1}$ region,[35,95] which is a fingerprint for Fe–O bond vibrations in the $Fe_2O_3$ and $CuFe_2O_4$ phases.[35] Following the electrocatalytic detection of glucose in a basic medium (the modified electrode after detection), significant spectral changes are observed. The notable decrease in the O–H band intensity and, more importantly, the clear alteration in the shape and intensity of the Fe–O band indicate a direct involvement of the metal oxide components in the reaction mechanism. This suggests that the oxidation of glucose is facilitated by a redox process involving the $Fe^{2+}$/$Fe^{3+}$ couples at the catalyst surface, consistent with the behavior of spinel ferrites in non-enzymatic sensing[5,21] Furthermore, the emergence of new features in the 1000–1200 $cm^{-1}$ region may be attributed to C–O bonds from adsorbed reaction

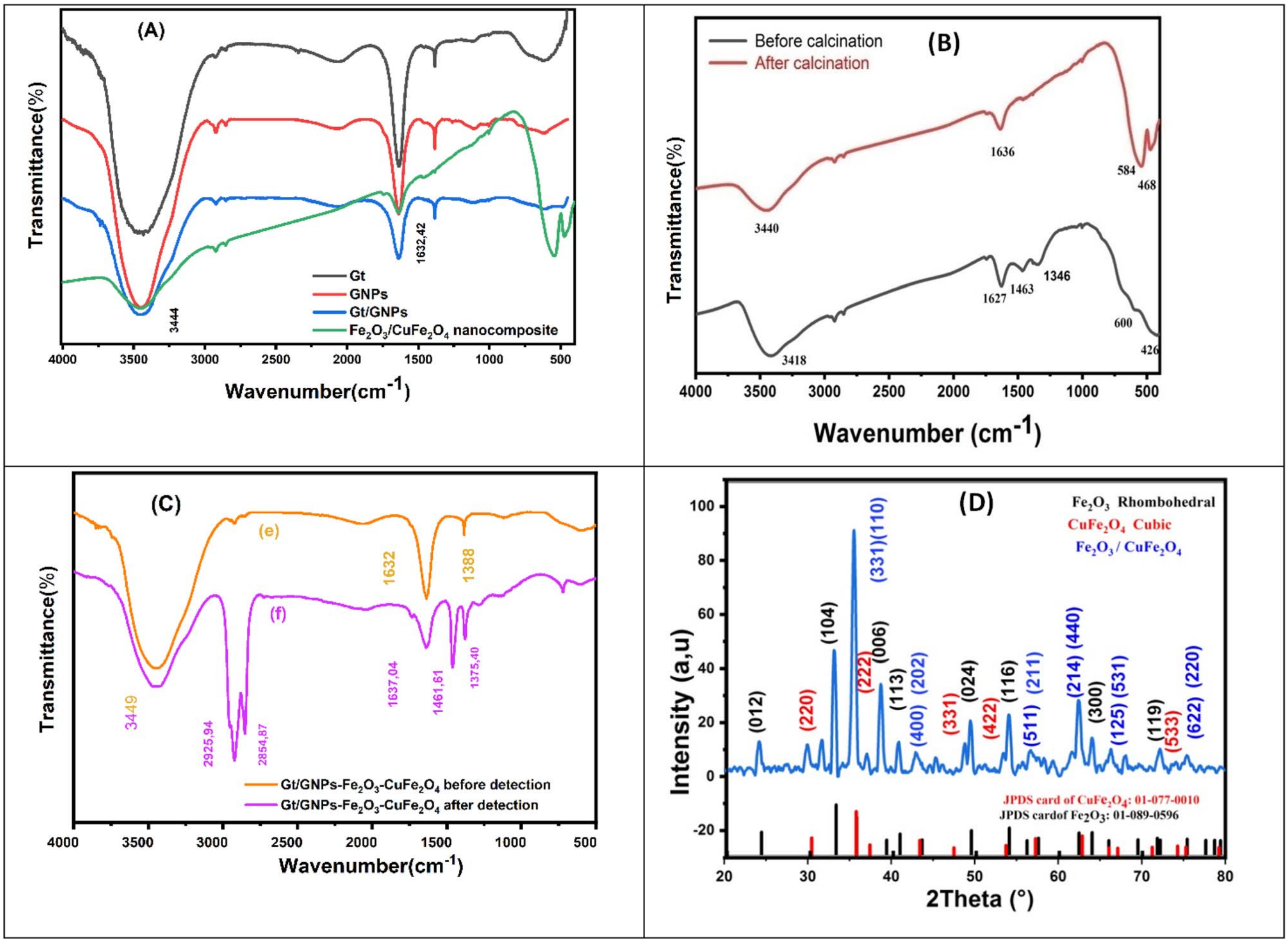

Fig. 1 FTIR spectrum of (A) FTIR spectra of Graphite, GNPs, Gt/GNPs, $Fe_2O_3/CuFe_2O_4$ (nanocomposite), (B) $Fe_2O_3/CuFe_2O_4$ nanocomposite before and after calcination. (C) $Fe_2O_3/CuFe_2O_4$/GNPs/Gt before and after glucose detection. (D) XRD spectra of the $Fe_2O_3/CuFe_2O_4$ nanocomposite.

intermediates or products, such as gluconolactone or gluconic acid. These results collectively verify that the metal oxides serve as the active sites and undergo specific chemical changes during the electrocatalytic detection of glucose.

From the FTIR spectrum of the $Fe_2O_3/CuFe_2O_4$ heterostructure synthesized and annealed at 630 °C presented in Fig. 1B, the broad absorption bands observed at 3440 $cm^{-1}$ and 1638 $cm^{-1}$ correspond to the O–H stretching and bending vibrations, respectively, indicating the presence of adsorbed water molecules on the surface of the nano-ferrite material.[97,104] The Two peaks observed in FTIR spectra $Fe_2O_3/CuFe_2O_4$ heterostructure before calcination at 1346 and 1463 $cm^{-1}$ may be due to residual nitrates, acetates, or organic precursors (from synthesis reagents like metal nitrates, chlorure or citrates). These bands disappear or weaken, confirming the thermal decomposition of residual precursors.[82]

The characteristic metal–oxygen vibrational bands appear in the low-wavenumber region, which are indicative of the spinel ferrite phase.[21] Specifically, the absorption peaks located at 584 $cm^{-1}$ and 468 $cm^{-1}$ are attributed to the stretching vibrations of Fe–O bonds in the tetrahedral and octahedral sites of the spinel lattice, respectively.[21] The peaks in the 400–700 $cm^{-1}$ range (attributed to Fe–O and Cu–O bonds) are typically broader and less distinct, indicating amorphous or poorly crystalline metal oxide phases. These become stronger and sharper, confirming the formation of the spinel crystal structure of $CuFe_2O_4$ and $Fe_2O_3$. Indicates improved crystallinity and successful phase formation.[23]

Furthermore, the FTIR spectroscopy was employed to investigate the structural and chemical modifications occurring in the $Fe_2O_3/CuFe_2O_4$/GNPs/Gt nanocomposite before and after glucose detection (Fig. 1C). Prior to glucose exposure, the FTIR spectrum exhibited a broad absorption band around 3400 $cm^{-1}$, which corresponds to the O–H stretching vibrations of hydroxyl groups present in gum tragacanth and physically adsorbed water molecules. The characteristic band at 1632 $cm^{-1}$ is attributed to H–O–H bending vibrations or to the stretching of carbonyl (C═O) groups within the polysaccharide matrix. The peak at 1388 $cm^{-1}$ is associated with C–H and C–O deformation vibrations, while the absorption bands below 600 $cm^{-1}$ correspond to Fe–O and Cu–O stretching modes, confirming the presence of ferrite phases ($Fe_2O_3$ and $CuFe_2O_4$).

After interaction with glucose, distinct spectral changes were observed. The appearance of new bands at 2922 $cm^{-1}$ and 2854 $cm^{-1}$ can be ascribed to the asymmetric and symmetric stretching of C–H bonds in glucose. Moreover, the slight shift of the 1632 $cm^{-1}$ band, accompanied by the emergence of new peaks at 1456 $cm^{-1}$ and 1374 $cm^{-1}$, suggests the formation of interactions between the hydroxyl (–OH) and carbonyl (C═O) groups of glucose and the active sites on the nanocomposite surface. These modifications in peak position and intensity indicate effective glucose adsorption through hydrogen bonding or coordination with Fe and Cu ions. Overall, the FTIR findings confirm the strong affinity and chemical interaction between glucose molecules and the $Fe_2O_3$–$CuFe_2O_4$/GNPs/Gt nanocomposite, highlighting its suitability for glucose sensing applications.

The X-ray diffraction (XRD) analysis (Fig. 1D) shows that a heterostructured nanocomposite made of rhombohedral hematite ($\alpha$-$Fe_2O_3$) and cubic spinel copper ferrite ($CuFe_2O_4$) has been successfully formed.[33] The diffraction peaks at $2\theta$ = 24.13°, 33.12°, 39.22°, 49.42°, 54.01°, 63.97°, and 72.18° match the (012), (104), (006), (024), (116), (300), and (119) crystallographic planes of $\alpha$-$Fe_2O_3$ (JCPDS card no. 01-089-0596), which shows that it has a rhombohedral structure. The peaks at $2\theta$ = 30.17°, 35.6°, 37.18°, 43.48°, 47.30°, 53.59°, 56.13°, 62.46°, 65.98°, 74.24°, and 75.43° are linked to the (220), (311), (222), (400), (331), (422), (511), (440), (531), (533), and (622) planes of cubic spinel $CuFe_2O_4$ (JCPDS card no. 01-077-0010).[119] Several peaks show overlapping reflections (for example, 35.6°/35.6°, 43.48°/43.2°, 56.13°/57.13°, 62.46°/62.75°), which means that both phases are present and that a well-integrated heterostructure has formed. The lack of impurity peaks suggests that the phase is very pure, and the sharp, well-defined peaks suggest that the crystals are very crystalline, which is important for better electrocatalytic performance in sensor applications.

The nanocomposite ($Fe_2O_3$/$CuFe_2O_4$) scanning electron microscope (SEM) analysis (Fig. 2A) revealed the presence of irregularly shaped nanoparticles forming aggregated clusters.[34] The images were captured at an accelerating voltage of 15 kV with magnifications ranging from 5000× to 100 00× and horizontal field widths (HFW) between 41.4 µm and 82.9 µm, providing detailed insight into the surface morphology of the nanocomposite.[26]

Complementary Energy-Dispersive X-ray Spectroscopy (EDX) approved the elemental composition (see Fig. 2B), indicating 62.24 wt% Fe, 15.46 wt% O, and 22.27 wt% Cu.[23] The corresponding atomic percentages were 45.85% Fe, 39.74% O, and 14.41% Cu.[23] The high content of Fe and O is consistent with the formation of $Fe_2O_3$, while the significant presence of Cu confirms the incorporation of $CuFe_2O_4$ (ref. 33). These results collectively verify the successful synthesis of a biphasic $Fe_2O_3$/$CuFe_2O_4$ nanocomposite, with both phases well-represented in the final material.

**3.1.1. Raman spectroscopy.** Raman spectroscopy was conducted to investigate the structural and compositional evolution across the synthesized materials (Fig. 3). The spectrum of graphite (Gt) showed a sharp G-band at ~1580 $cm^{-1}$ and a negligible D-band at ~1350 $cm^{-1}$, reflecting a highly crystalline $sp^2$ carbon structure with minimal defects.[75] In contrast, graphene nanoplatelets (GNPs) exhibited a pronounced D-band and a broadened G-band with a significantly higher $I_D/I_G$ ratio, indicating the introduction of lattice defects and residual oxygen-containing functional groups during oxidation and the subsequent incomplete reduction process.[51] The Gt/GNPs hybrid displayed intermediate characteristics, with a notably increased D-band intensity compared to graphite, suggesting interfacial strain and defect formation at the junctions between the graphitic and graphene nanoplatelets domains.[59]

The $Fe_2O_3$/$CuFe_2O_4$ precursor before calcination showed only broad, poorly resolved Raman features in the 200–700 $cm^{-1}$ range, indicative of amorphous or poorly crystalline metal–oxygen vibrational modes.[36] After calcination, these features sharpened dramatically into a well-defined set of

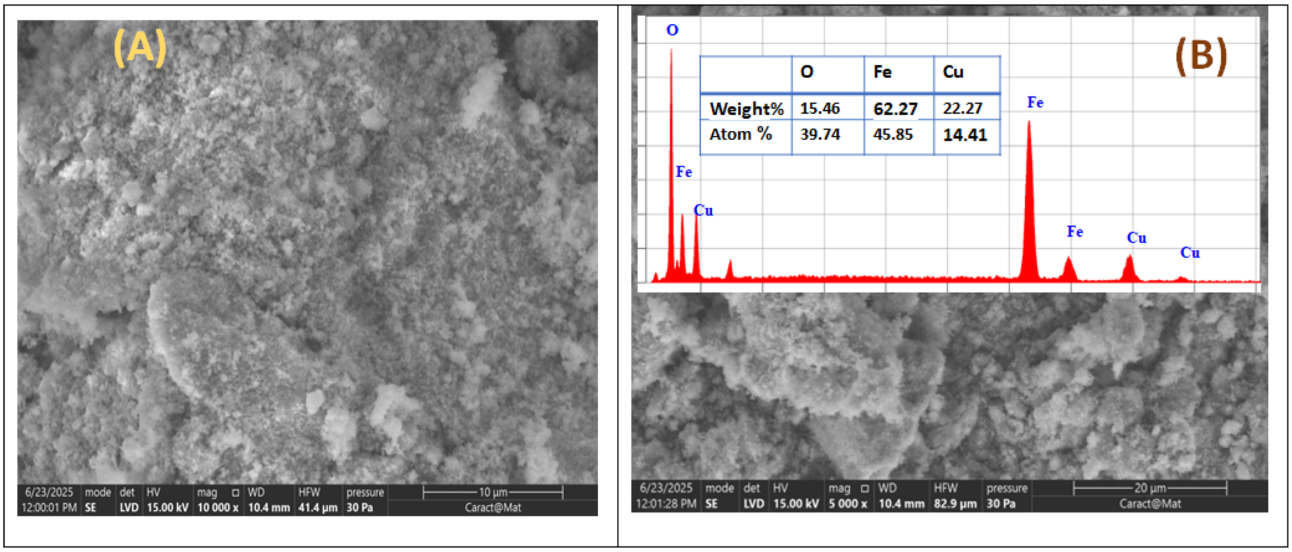

| | O | Fe | Cu |
|---|---|---|---|
| Weight% | 15.46 | 62.27 | 22.27 |
| Atom % | 39.74 | 45.85 | 14.41 |

Fig. 2 SEM image of (A) the $Fe_2O_3$/$CuFe_2O_4$ nanocomposite and (B) EDX spectra of $Fe_2O_3$/$CuFe_2O_4$.

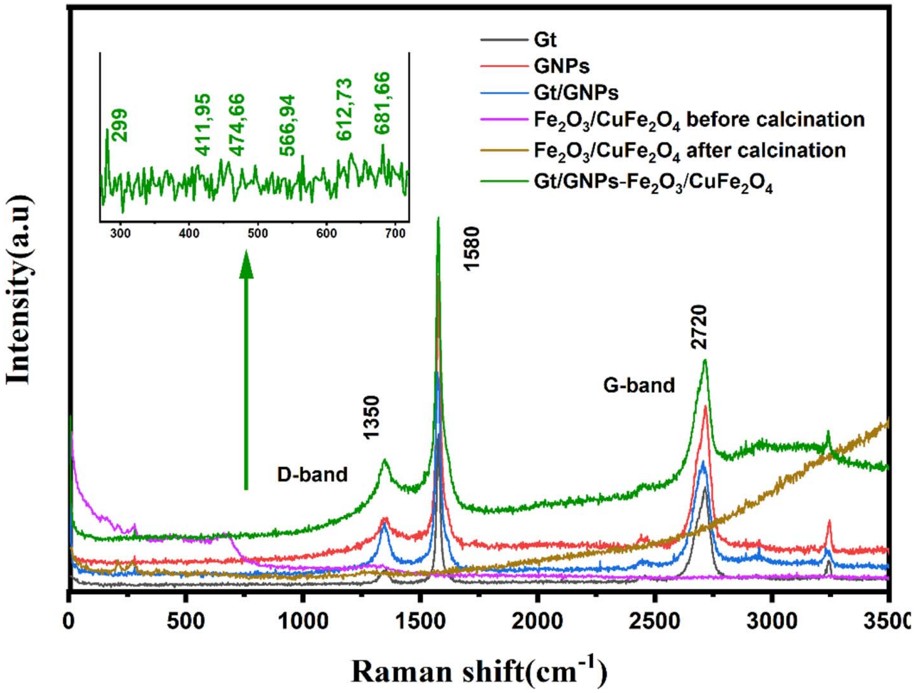

Fig. 3 Raman spectra of Graphite, GNPs, Gt/GNPs, $Fe_2O_3/CuFe_2O_4$ (before and after calcination), and Gt/GNPs-$Fe_2O_3/CuFe_2O_4$ nanocomposite.

peaks. A precise spectral assignment confirms the formation of the target crystalline phases: the peaks at 299, 412, and 613 cm$^{-1}$ are unambiguous signatures of hematite ($\alpha$-$Fe_2O_3$), corresponding to $E_g$ and $A_{1g}$ vibrational modes.[126] Concurrently, the peaks at 475, 567, and 682 cm$^{-1}$ are diagnostic of the spinel structure, confirming the successful synthesis of copper ferrite ($CuFe_2O_4$).[76] The coexistence of these distinct bands confirms the formation of a binary metal oxide system. Additionally, the calcined sample exhibited a significant fluorescence background in the higher wavenumber region (>3000 cm$^{-1}$), attributed to charge recombination within the semiconductor oxides and possibly surface –OH groups.[9] In the final $Fe_2O_3/CuFe_2O_4$/GNPs/Gt composite, the carbon D- and G-bands remained prominent, indicating the survival of the graphene-based network, albeit with a substantial defect density.[30,51] Crucially, the Raman spectrum retained the distinct low-wavenumber bands of both crystalline $\alpha$-$Fe_2O_3$ and spinel $CuFe_2O_4$, providing direct evidence for the successful integration of these metal oxide nanoparticles within the carbon matrix without phase degradation.[30,109] The further increased D-band intensity and broadening of the carbon signals, relative to the Gt/GNPs hybrid, suggest strong interfacial interactions between the carbon substrate and the metal oxides. This interaction likely induces local strain and facilitates charge transfer, contributing to the enhanced disorder.[13,59]

**3.1.2. X-ray photoelectron spectroscopy (XPS) analysis.** X-ray photoelectron spectroscopy (XPS) was employed to investigate the surface composition and oxidation states of the $Fe_2O_3/CuFe_2O_4$ nanocomposite immobilized on graphite (Gt) sheets/graphene nanoplatelets (GNPs) (Fig. 4). The wide-scan spectra were collected using a Mg K$\alpha$ radiation source (1253.6 eV) with a step size of 1.0 eV and a pass energy of 50 eV, covering a binding energy range of 0–1000 eV to identify the elemental composition of the samples. The investigated systems included S01 (Gt/GNPs), S02 ($Fe_2O_3/CuFe_2O_4$), S03 ($Fe_2O_3/CuFe_2O_4$/GNPs/Gt nanocomposite before electrochemical use), and S04 ($Fe_2O_3/CuFe_2O_4$/GNPs/Gt nanocomposite after glucose detection in NaOH solution). In addition to the survey scans, high-resolution spectra were recorded for the Fe 2p, Cu 2p, and O 1s regions. Peak deconvolution was carried out using Gaussian–Lorentzian fitting with Shirley background subtraction to resolve chemical states and distinguish surface oxidation environments, following established protocols in XPS data analysis[12] NIST X-ray Photoelectron Spectroscopy Database. The use of XPS in nanomaterial characterization has been widely reported, with recent reviews highlighting its role in probing 2D materials for oxidation/corrosion protection,[88] graphene-based sensing systems,[112] and carbon nanotube/graphite hybrid structures.[120] These studies reinforce the significance of XPS as a robust technique for linking chemical states with functional performance in nanostructured composites.

**3.1.3. C 1s high-resolution analysis.** High-resolution C 1s spectra provide insights into the carbon bonding environments as shown in Fig. 5A. For sample (Fig. 5A(a)), likely corresponding to the Gt/GNPS composite, the deconvoluted peaks at 276.61 eV, 285.76 eV, and 284.97 eV are assigned to C–C/C═C (sp$^2$ hybridized carbon),[6,84] C–O (epoxy/hydroxyl groups),[25,125] and adventitious carbon, respectively, with the dominant peak at ~285 eV indicating a graphitic structure with oxygenated defects.[25,125] In sample (Fig. 5A(b)), peaks at 284.95 eV and

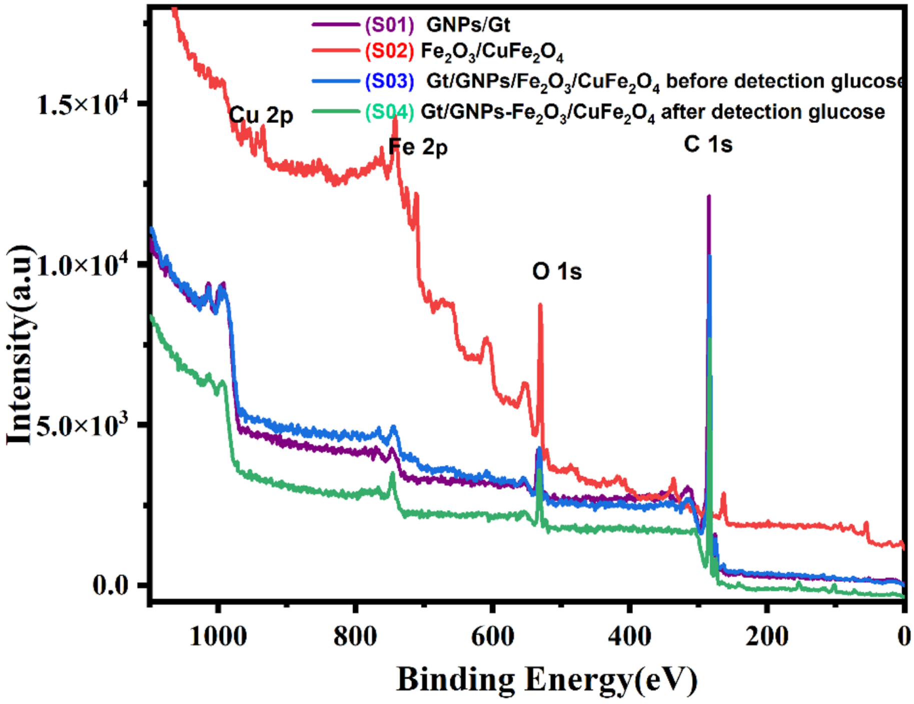

Fig. 4 Wide-scan XPS spectra of (S01) Gt/GNPs, (S02) $Fe_2O_3/CuFe_2O_4$, (S03) Gt/GNPs/$Fe_2O_3/CuFe_2O_4$ nanocomposite before use, and (S04) Gt/GNPs-$Fe_2O_3/CuFe_2O_4$ nanocomposite after glucose detection. Overlaid comparison shows attenuation of metal signals in (S04).

285.83 eV suggest a shift toward higher binding energies, implying increased oxidation or interaction with metal oxides.[50] Sample (Fig. 5A(c)) shows a single broad peak at 286.123 eV, which may reflect further carbon oxidation or contamination after glucose detection.[7] These shifts highlight the role of graphene in stabilizing the nanocomposite[50,98] while undergoing minor surface alterations during sensing.[7]

**3.1.4. Fe 2p high-resolution analysis.** As shown in Fig. 5B, the Fe 2p spectrum in (S02, Fig. 5B(a)) exhibits a doublet at Fe $2p_{3/2}$ (∼710.8 eV) and Fe $2p_{1/2}$ (∼724 eV) with a satellite at ∼718 eV, indicating $Fe^{3+}$ in $Fe_2O_3$ (FWHM ∼2.5 eV).[15] The 2p orbital splits into $2p_{3/2}$ (higher intensity, $j = 3/2$ state with three spin orientations) and $2p_{1/2}$ (lower intensity, $j = 1/2$ state with one spin orientation) due to spin–orbit coupling, with a splitting energy of ∼13 eV typical for Fe[113] Deconvolution reveals ∼68% $Fe^{3+}$ and ∼32% $Fe^{2+}$, consistent with spinel $CuFe_2O_4$ structures.[52] In (S03, Fig. 5B(b)), intensity decreases (∼50%) due to graphite encapsulation, with a minor shift to ∼711 eV from surface OH adsorption.[37] In (S04, Fig. 5Bc), further attenuation (<20% of S02) and shift to ∼711.5–712 eV (FWHM ∼10 eV) confirm FeOOH formation (∼20% contribution) and increased $Fe^{2+}$ (∼35%), arising from redox cycling during glucose oxidation ($Fe_2O_3 + OH^- \rightarrow FeOOH + e^-$).[5] The $2p_{3/2}$ peak dominates (∼70% of the doublet intensity) as it has higher degeneracy, providing sensitive probing of Fe oxidation states. The $Fe^{3+}/Fe^{2+}$ ratio (∼2 : 1 in S02) decreases to ∼1.9 : 1 in (S03) and ∼1.7 : 1 in (S04, Fig. 5B(c)), reflecting progressive reduction during activation and reaction, which enhances catalytic activity by balancing oxidative power and electron transfer.[52,60]

**3.1.5. Cu 2p high-resolution analysis.** In Fig. 5C, (S02, Fig. 5C(a)) shows Cu $2p_{3/2}$ (∼933.5 eV) and Cu $2p_{1/2}$ (∼952 eV) with shake-up satellites (∼941–943 eV, ∼40% intensity), confirming $Cu^{2+}$ in $CuFe_2O_4$ (∼80%) with minor $Cu^+$ (∼20%). The 2p splitting arises from spin–orbit coupling, with $2p_{3/2}$ ($j = 3/2$, higher intensity) and $2p_{1/2}$ ($j = 1/2$, ∼50% intensity of $2p_{3/2}$) separated by ∼19 eV, characteristic of Cu's $d^{10}$ configuration in $Cu^+$ *vs.* $d^9$ in $Cu^{2+}$ (evident from satellite presence).[14,37] (S03, Fig. 5C(b)) exhibits reduced intensity (∼60%) and a shift to ∼934 eV from graphite interaction.[113](S04, Fig. 5C(c)) displays severe attenuation (<10%) and a shift to ∼934.5–935 eV, with weakened satellites and increased $Cu^+$ (∼25%), indicating CuOOH formation ($CuO + OH^- \rightarrow CuOOH + e^-$) and $Cu^{2+}/Cu^{3+}$ cycling[60]

**3.1.6. O 1s high-resolution analysis.** In Fig. 5D, S02 (Fig. 5D(a)) shows lattice $O^{2-}$ (∼529.5–530 eV, ∼60%) and surface-adsorbed OH groups (∼531 eV, ∼40%)[37,113] S03 (Fig. 5D(b)) shifts to ∼530–531 eV (∼5000 cps) with a significant increase in the OH component (∼50%) resulting from NaOH activation.[52,113] S04 (Fig. 5D(c)) broadens to ∼531–533 eV (∼6000 cps), deconvoluting to ∼25% lattice $O^{2-}$, ∼55% metal-OH (FeOOH/CuOOH), ∼15% O–C (from adsorbed gluconic acid), and ∼5% $H_2O$, confirming the role of hydroxide mediation and organic deposition during the glucose oxidation process.[60]

**3.1.7. Na 1s high-resolution analysis.** In Fig. 5E, the high-resolution XPS analysis of the Sodium (Na 1s) core level reveals four distinct spectral components (M1–M4), indicating the presence of sodium in multiple chemical states within the sample. The most prominent feature is the highly intense M3 peak centered at a binding energy of 1070.7 eV. This value is characteristic of $Na^+$ ions in a stable configuration, strongly suggesting that this component corresponds to sodium bound to the gluconate molecule, effectively representing the sodium gluconate salt which acts as a counterion to the organic carboxylate group.

The other components are attributed to surface-related species. The low binding energy component at 1065.4 eV (M2) are likely associated with highly oxidized species or surface contaminants, such as NaOH or $Na_2O$. In contrast, the higher binding energy peaks at 1076.23 eV (M3) and 1079.42 eV (M4) are often indicative of plasmon loss features or differential charging effects, though they may also represent $Na^+$ ions in highly electronegative environments or associated with lattice defects.

This analysis confirms the successful incorporation of the gluconate salt into the composite structure.

The XPS results demonstrate successful nanocomposite formation (S03) and surface evolution post-glucose detection (S04), with metal attenuation and OH/O–C increases indicating catalytic activity. The $2p_{3/2}$ and $2p_{1/2}$ peaks provide detailed insights into oxidation states, with $2p_{3/2}$'s higher intensity enabling precise deconvolution of $Fe^{3+}/Fe^{2+}$ and $Cu^{2+}/Cu^+$ ratios. Post-use XPS (S04) correlates with enhanced performance: OH intermediates (O 1s ∼531 eV) mediate oxidation, while passivation slightly reduces long-term stability but maintains initial efficiency.

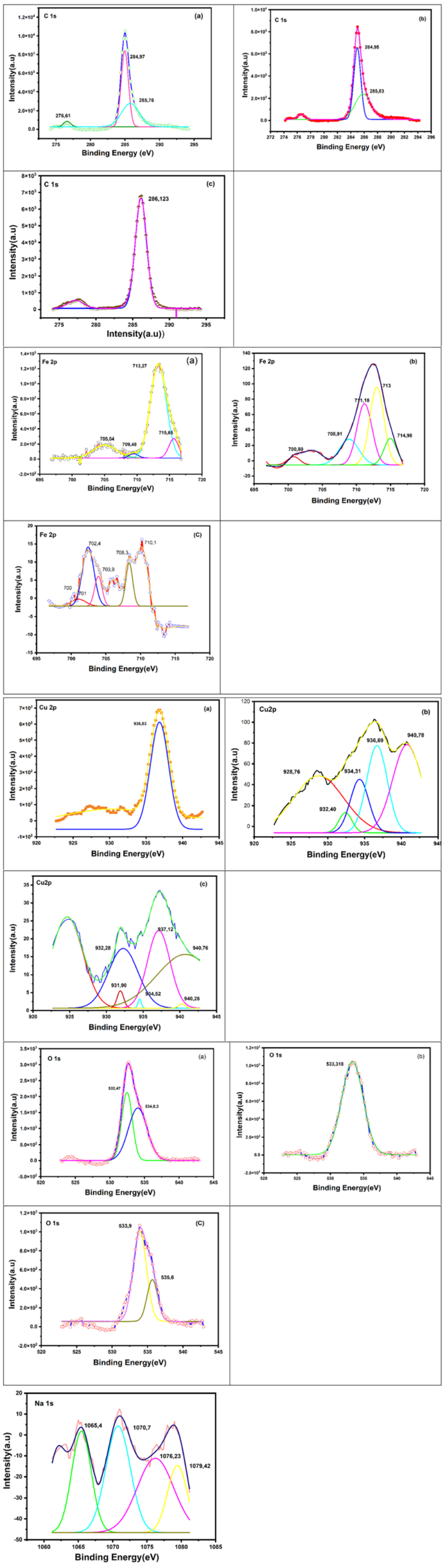

Fig. 5 (A): High-resolution C 1s spectra: (a) (S01), (b) (S03), (c) (S04) showing deconvoluted components for C–C/C–H (∼284.9–285.0 eV) and C–O (∼285.7–286.1 eV), indicating increased carbon oxidation. (B): High-resolution Fe 2p spectra: (a) (S02), (b) (S03), (c) (S04) with deconvolution showing $Fe^{3+}$ ($2p_{3/2}$ ∼710.8 eV, $2p_{1/2}$ ∼724 eV), $Fe^{2+}$, and FeOOH components. Inset: Spin–orbit splitting diagram for Fe 2p, with $Fe^{3+}/Fe^{2+}$ ratio evolution. (C): High-resolution Cu 2p spectra: (a) (S02), (b) (S03), (c) (S04) with deconvolution showing $Cu^{2+}$ ($2p_{3/2}$ ∼933.5 eV, $2p_{1/2}$ ∼952 eV with satellites), $Cu^+$, and CuOOH components. Inset: Spin–orbit splitting for Cu 2p, highlighting satellite for $Cu^{2+}$. (D): High-resolution O 1s spectra: (a) (S02), (b) (S03), (c) (S04) with deconvolution showing lattice O, OH, O–C, and $H_2O$ components. (E): High-resolution Na 1s spectra: (S04) with deconvolution.

## 3.2. Electrochemical characterization

Electrochemical characterizations were performed by using CV and EIS techniques for the different modified electrodes.

### 3.2.1. Performance of graphene/graphite ratios.

Graphene nanoplatelets (GNPs) was used as a conductivity enhancer in carbon paste electrodes (CPEs), and its content significantly influenced the electrode's performance was investigated using a mixture solution containing 0.1 M KCl and 5 mM $[Fe(CN)_6]^{3-/4-}$ and electrochemical measurements by CV and EIS techniques. The redox couple was employed to evaluate the electron transfer behavior of electrodes prepared with various graphene-to-graphite mass ratios (0, 5, 10, 15, 20, 25, 30, 35, 40, 45, 50, and 100%), as illustrated in Fig. 6.

The electrochemical performance of electrodes with varying graphene nanoplatelets (GNPs) to graphite ratios was evaluated to identify the composition with the lowest charge transfer resistance and highest redox activity. While both graphite and GNPs are conductive carbon materials, they exhibit different physical and electronic properties. Graphite provides structural robustness and moderate conductivity, whereas GNPs offer high electron mobility,[2,16] and a large surface area. However, excessive GNPs content can lead to restacking and aggregation,

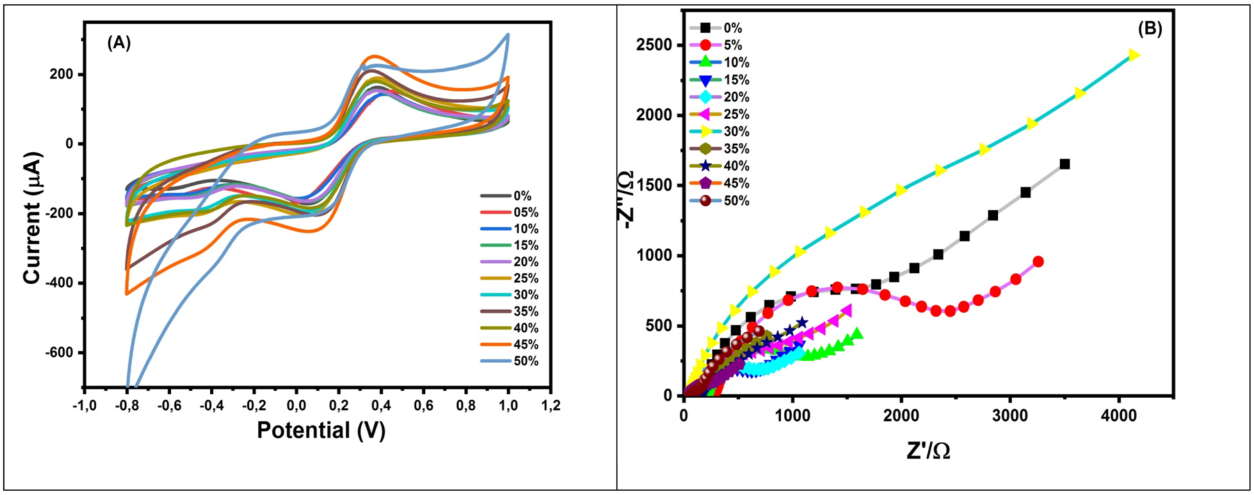

Fig. 6 (A) Cyclic voltammograms (B) Nyquist diagram of different percentages of graphite/GNPs (0, 5, 10, 20, 25, 30, 35; 40, 45, 50, 100 wt%) in a solution containing 5 mM Fe(CN)$_6^{3-/4-}$ and 0.1 M KCl.

reducing electroactive surface area and conductivity due to poor dispersion[2,125]

The unmodified electrode (0% GNPs) exhibited the lowest redox peak current[16,17] (Fig. 6A). In contrast, all GNPs-modified electrodes showed enhanced redox responses[16,17] Increasing the GNPs content resulted in a gradual rise in both anodic and cathodic peak currents, as summarized in Table 1a.[125] Notably, the electrode with a 45 : 55 GNPs -to -graphite ratio[116] demonstrated the highest oxidation peak current (290.8 μA) and the smallest peak potential separation ($\Delta E_p$), indicating rapid electron transfer kinetics.[42] Furthermore, the peak current ratio ($I_{pa}/I_{pc}$) of 1.11 suggests a reversible redox process.[11] The superior electrical conductivity of GNPs is likely responsible for the enhanced electrochemical performance of the modified CPEs[42] Based on these results, the optimal GNPs-to- graphite ratio for electrode fabrication was determined to be 45 : 55.[116] Nyquist plots for bare graphite and GNPs/graphite modified with different wt% were recorded, as shown in Fig. 5B and Table 1a. Each EIS [53] spectrum consists of two regions: a quasi-semicircular portion at high frequencies and a linear segment at low frequencies. The diameter of the semicircular region corresponds to the charge transfer resistance ($R_{ct}$), with a larger diameter indicating a higher $R_{ct}$.[17,42] Conversely, the near-vertical linear portion reflects efficient electron transfer at the electrode interface.[53] The $R_{ct}$ values for various GNPs to graphite mass ratios (0, 5, 10, 15, 20, 25, 30, 35, 40, 45, 50, and 100%)

Table 1 Electrochemical data from CV and EIS measurements obtained from the electrodes modified with (A) GNPs/graphite ratios and (B) $Fe_2O_3/CuFe_2O_4$ wt%. The data are obtained from the voltammetric and impedimetric experiments (Fig. 5 and 6)

| | $I_a$ (mA) | $I_c$ (mA) | $E_{oxd}$ (V) | $E_{red}$ (V) | $E_{1/2}$ (V) | $R_s$ (Ω) | $R_{ct}$ (Ω) | $Q$ μF | $W$ (Ω) |
|---|---|---|---|---|---|---|---|---|---|
| **(A) GNPs/Graphite ratio** | | | | | | | | | |
| 0 | 0.163 | −0.171 | 0.380 | −0.1712 | 0.104 | 148.6 | 1675 | 24.49 | 1453 |
| 5:95 | 0.152 | −0.171 | 0.447 | −0.1713 | 0.137 | 282.5 | 2110 | 21.26 | 725 |
| 10 : 90 | 0.143 | −0.156 | 0.415 | −0.1562 | 0.129 | 197.9 | 977.7 | 47.88 | 351.8 |
| 15 : 85 | 0.154 | −0.164 | 0.372 | −0.1647 | 0.103 | 106.1 | 586.1 | 67.44 | 304.7 |
| 20 : 80 | 0.153 | −0.164 | 0.381 | −0.1643 | 0.108 | 66.06 | 660.8 | 57.27 | 266.6 |
| 25 : 75 | 0.190 | −0.206 | 0.384 | −0.206 | 0.089 | 80.05 | 931.9 | 95.21 | 495.0 |
| 30 : 70 | 0.179 | −0.193 | 0.375 | −0.1936 | 0.090 | 42.13 | 2983 | 65.26 | 1784 |
| 35 : 65 | 0.210 | −0.204 | 0.353 | −0.204 | 0.074 | 71.32 | 261.9 | 287.8 | 480.6 |
| 40 : 60 | 0.180 | −0.184 | 0.374 | −0.184 | 0.095 | 146.6 | 436.7 | 253.6 | 598.7 |
| 45 : 55 | 0.290 | −0.260 | 0.330 | −0.2606 | 0.035 | 32.04 | 151.2 | 245.6 | 194.6 |
| 50 : 50 | 0.225 | −0.227 | 0.318 | −0.2272 | 0.045 | 56.7 | 259.0 | 140.9 | 432.6 |
| **(B) $Fe_2O_3/CuFe_2O_4$-wt%** | | | | | | | | | |
| 1 | 0.2096 | −0.2083 | 0.3752 | 0.0656 | 0.2204 | 46.14 | 269.7 | 246.9 | 182.8 |
| 3 | 0.2204 | −0.2281 | 0.3723 | 0.0618 | 0.2170 | 41.08 | 285.6 | 215.0 | 286.3 |
| 5 | 0.271 | −0.2551 | 0.327 | 0.09277 | 0.2098 | 26.29 | 181.1 | 291.2 | 303.3 |
| 7 | 0.2451 | −0.2464 | 0.3715 | 0.05369 | 0.2125 | 31.02 | 451.7 | 306.2 | 589.6 |
| 9 | 0.213 | −0.2229 | 0.3767 | 0.05091 | 0.2138 | 39.19 | 367.4 | 213.3 | 296.4 |
| 10 | 0.2721 | −0.2325 | 0.3202 | 0.1279 | 0.2240 | 42.37 | 77.7 | 230.5 | 266.4 |

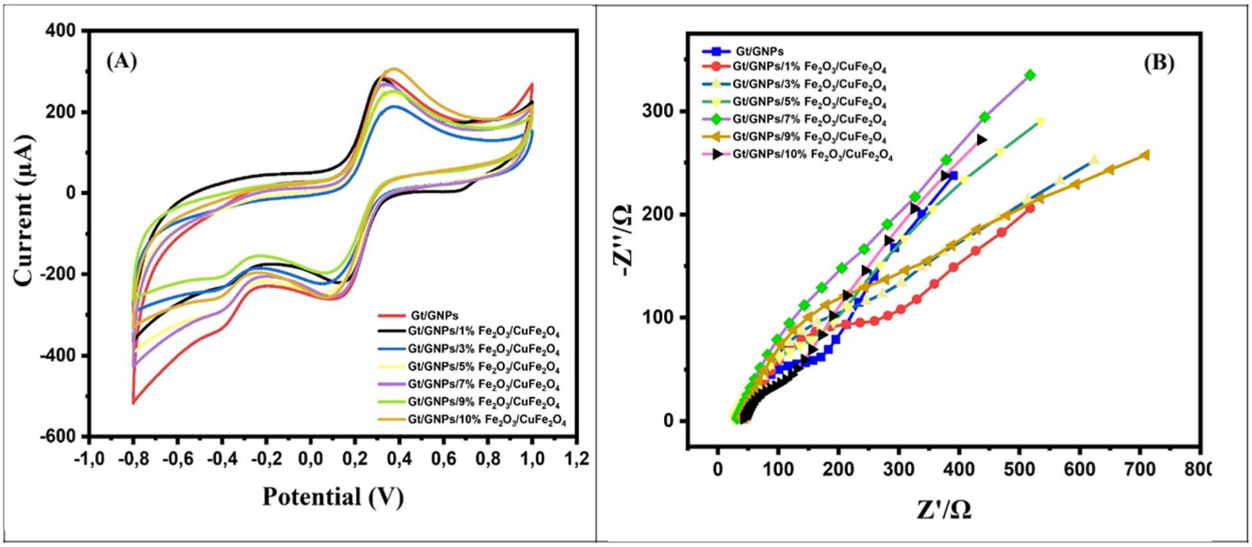

Fig. 7 (A) Cyclic voltammograms (B) Nyquist diagram of different percentages of $Fe_2O_3/CuFe_2O_4$ (1; 03, 05, 07; 09; 10 wt%) in a solution containing 5 mM $Fe(CN)_6{}^{3-/4-}$ and 0.1 M KCl.

electrodes were recorded as shown in Table 1. The electrode with a 45 : 55 GNPs-to-graphite ratio demonstrated the lowest $R_{ct}$ value (151.2 Ω) which matched with the CV measurements. In contrast, the GNPs/graphite modified electrode (45 : 55%) significantly enhanced electron transfer kinetics.

The optimized ratio of 45 : 50 (GNPs : graphite) was found to balance these effects.[78] This composition lies near the percolation threshold, where a continuous conductive network forms due to optimal GNPs interconnectivity while maintaining structural support from graphite.[17,78,116] Compared to the 50 : 50 ratio, the 45 : 55 ratio yielded slightly lower $R_{ct}$ values and better peak current responses, suggesting improved electron mobility and charge transport efficiency. Ratios with higher GNPs content (>60%) led to unstable electrochemical responses, likely due to poor dispersion.[83] These findings indicate a synergistic effect between graphite and GNPs, enhancing both mechanical integrity and electron transport within the composite. Moreover, the EIS interpretation (*i.e.* semicircle → $R_{ct}$) is consistent with analogous results in composite.[85]

### 3.2.2. Electrochemical performance of $Fe_2O_3/CuFe_2O_4$ ratio in $Fe_2O_3/CuFe_2O_4$ /GNPs/Gt nanocomposites.

To optimize the amount of active metal oxide phase, various loadings of $Fe_2O_3/CuFe_2O_4$ (1–10 wt%) were incorporated into the carbon matrix. The electrochemical behavior of a GNPs/graphite nanocomposite (mass ratio 45 : 55) modified with varying amounts (1, 3, 5, 7, 9, and 10 wt%) of $Fe_2O_3/CuFe_2O_4$ was investigated using CV and EIS in redox solution ferro/ferri cyanide. CV measurements at a scan rate of 50 mV $s^{-1}$ for bare Gt, Gt/GNPs, and$Fe_2O_3/CuFe_2O_4$/GNPs/Gt composites are shown in Fig. 7A and Table 1b.

The peak-to-peak separation ($\Delta E_p$, see Table 1) for GNPs/graphite electrode decreased compared with bare graphite electrode, reflecting improved electrical conductivity due to the presence of GNPs.[17,117] Among the tested materials, the $Fe_2O_3/CuFe_2O_4$/GNPs/Gt composite exhibited the lowest $\Delta E_p$ and the highest peak current ($I_p$), indicating enhanced electron transfer kinetics. This improvement is attributed to the excellent electrocatalytic[125] properties of $Fe_2O_3/CuFe_2O_4$, which, when optimally incorporated into the composite, significantly boosts the electrochemical response of the electrode.[4,79]

Nyquist plots for GNPs/graphite modified with (1, 3, 5, 7, 9, and 10 wt%) $Fe_2O_3/CuFe_2O_4$ were recorded, as shown in Fig. 7B and Table 1b. The GNPs/graphite modified with (10 wt%) $Fe_2O_3/CuFe_2O_4$ exhibited the lowest $R_{ct}$ value (77.7 Ω), indicating significantly enhanced electron transfer kinetics. At lower loadings (*e.g.*, 5% and 7%), the catalytic surface area was insufficient to generate a significant current, resulting in higher $R_{ct}$ values. At higher loadings (*e.g.*, 12.5% and 15%), the metal oxide nanoparticles tended to agglomerate, obstructing the carbon network and impeding electron flow.[87] This led to increased charge-transfer resistance and reduced electrochemical performance. The 10 wt% loading strikes an optimal balance between catalytic activity and conductive pathway integrity. The observed trend highlights a synergistic interaction between the metal oxide particles and the conductive carbon network, where sufficient redox-active sites are available without compromising the electron mobility across the electrode surface.

These EIS findings are in good agreement with the cyclic voltammetry results, further validating the improved electrochemical performance of the modified electrodes.[42]

To enhance the understanding of the electrochemical performance, the effective electrochemically active surface area (EASA) was determined for unmodified graphite electrodes, graphite/GNPs electrodes, and those modified with $Fe_2O_3/CuFe_2O_4$/GNPs/Gt nanocomposites.[103]

This evaluation was conducted by studying the influence of scan rates ranging from 10 to 250 mV $s^{-1}$, as illustrated in Fig. 8(A–C).

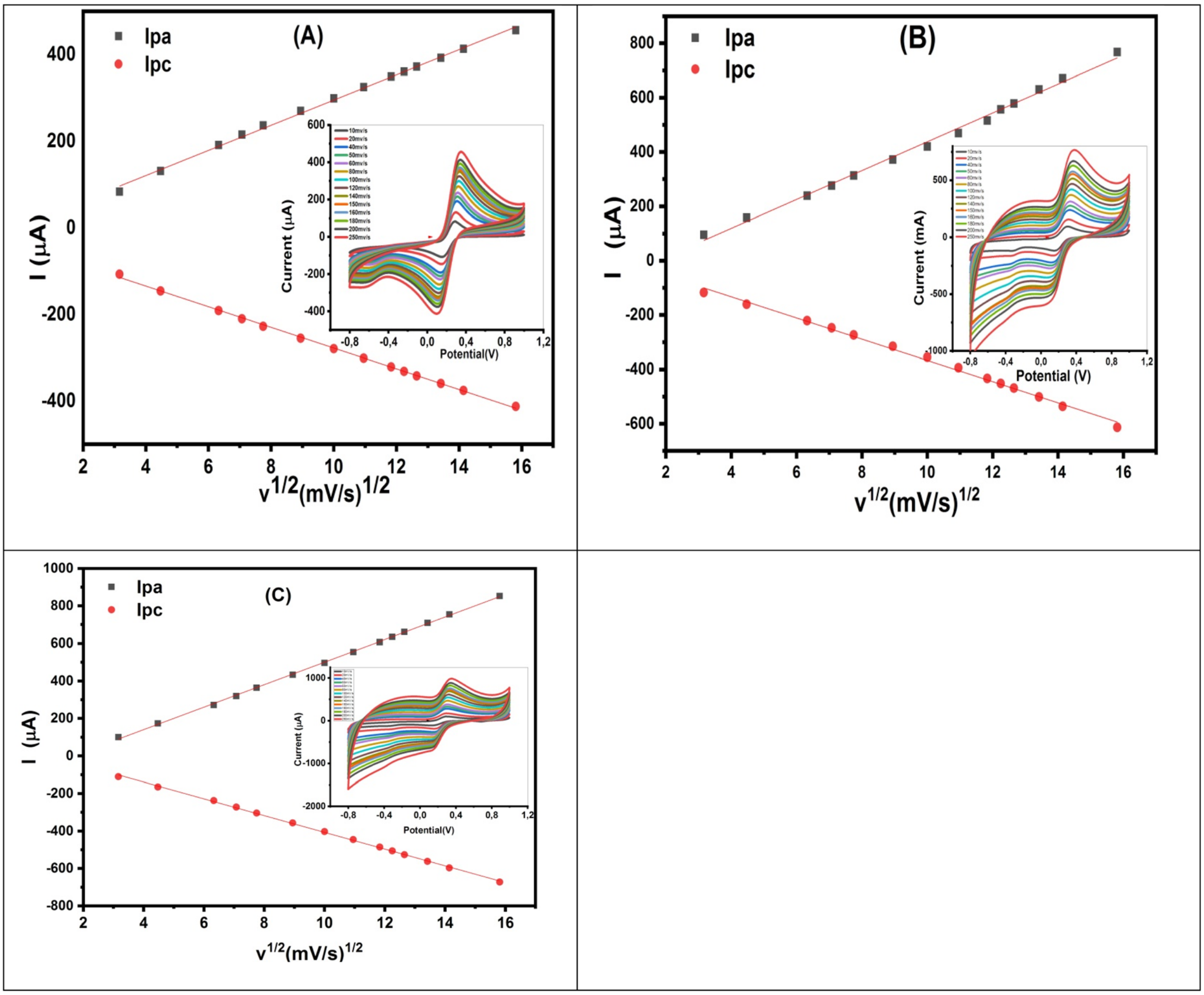

Fig. 8 Plots of peak current against the square root of scan rate and inset figures is cyclic voltammograms of (A) graphite, (B) graphite/GNPs, (C) $Fe_2O_3/CuFe_2O_4/GNPs/Gt$ in a 5 mM $Fe(CN)_6{}^{3-}/{}^{4-}$ solution containing 0.1 M KCl at varying scan rates.

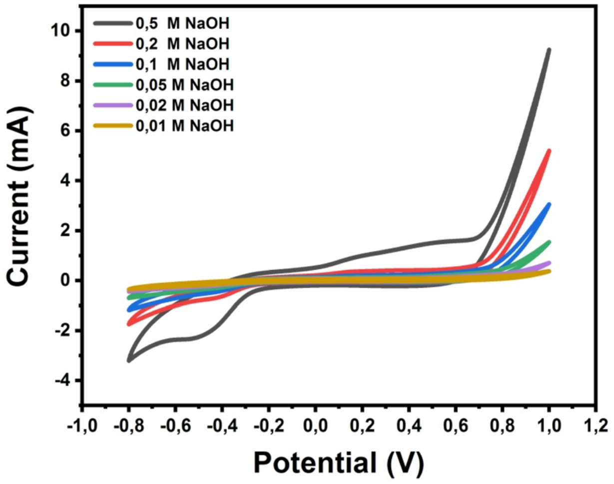

Fig. 9 Cyclic voltammograms of$Fe_2O_3/CuFe_2O_4/GNPs/Gt$ indifferent concentrations of NaOH solutions with 2.0 mM glucose at 50 mV $s^{-1}$ Ag/AgCl.

The relationship between the peak current and the square root of the scan rate was analyzed to assess the diffusion-controlled electrochemical behavior.[96] The active surface area for each electrode was calculated using the Randles–Ševčík eqn (1).[108] Which is commonly applied for reversible redox systems:[32]

$$I_P = 2.69 \times 10^5 \times \sqrt[3]{n} \times \mathrm{A} \times \sqrt{D} \times C \times \sqrt{\nu} \qquad (1)$$

where $I_p$ is the voltammetric peak current, $n$ is the number of electron transfer, $A$ is the electrochemical active surface area ($cm^2$), $D$ is the diffusion coefficient ($cm^2\ s^{-1}$), $C$ is the concentration of the electrochemical redox species $[Fe\ (CN)_6]^{3-/4-}$ (mol $l^{-1}$),and $\nu$ means the scan velocity (V $s^{-1}$).

By plotting $I_p$ *versus* the square root of the scan rate ($\nu^{1/2}$), the electroactive surface areas were calculated for each electrode type. The unmodified graphite electrode had an active area of 0.249 $cm^2$, while the graphite/GNPs and $Fe_2O_3/CuFe_2O_4/GNPs/Gt$ modified electrodes showed larger areas of 0.453 $cm^2$ and 0.511 $cm^2$, respectively.[96,103] This indicates that modification

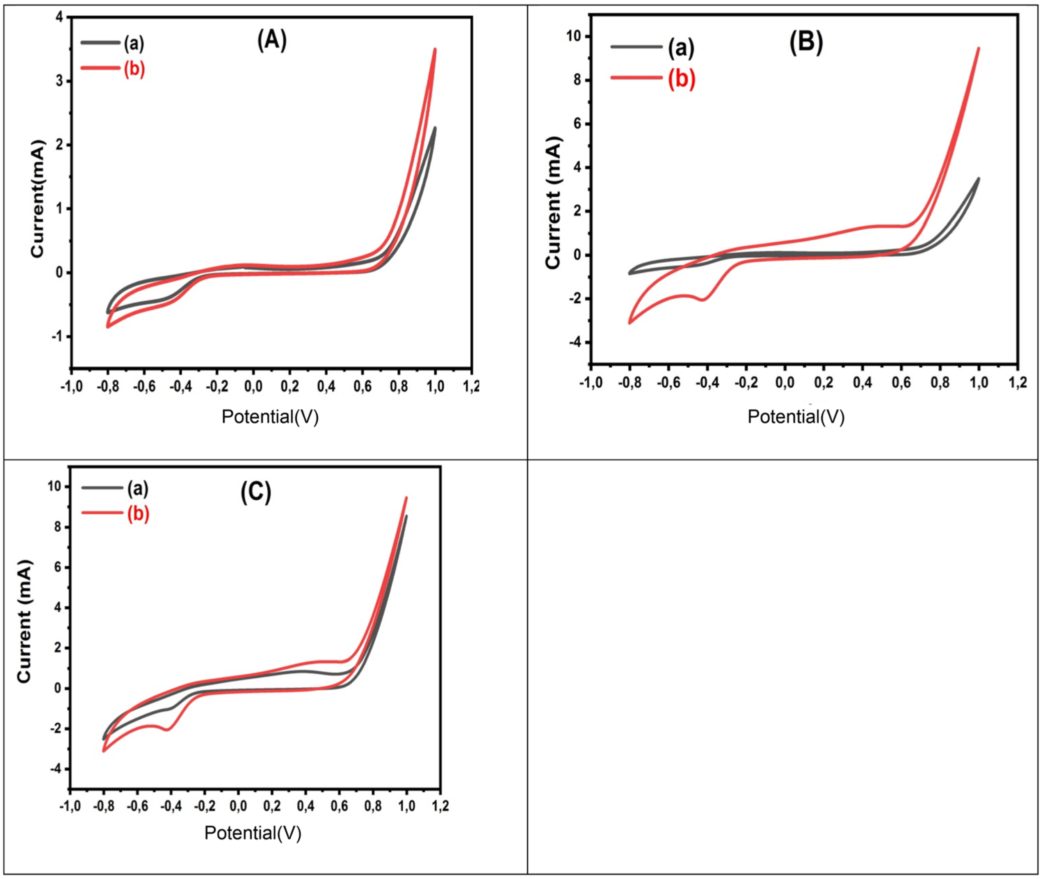

Fig. 10 Cyclic voltammograms of the (A) graphite, (B) graphite/graphene and (C) $Fe_2O_3/CuFe_2O_4$/GNPs/Gt in the (a) presence and (b) absence of 2 mM glucose. The electrolyte is 0.5 M NaOH and the scan rate is 50 mV $s^{-1}$.

with the nanocomposite significantly enhances the effective surface area available for electron transfer.[79]

Moreover, the nearly linear relationship between $I_p$ and $v^{1/2}$, particularly in the nanocomposite-modified electrode, suggests a diffusion-controlled process.[32] The observed peak separation also supports a quasi-reversible redox behavior.[4]

### 3.3. Optimization of NaOH concentration as electrolyte

The electrochemical activity of carbon paste sensors based on $Fe_2O_3/CuFe_2O_4$/GNPs/Gt composites was evaluated using cyclic voltammetry (CV) Fig. 9 in varying concentrations of NaOH (0.01, 0.02, 0.05, 0.1, 0.2, and 0.5 M), both in the presence of 2 mM glucose.[79] Measurements were conducted at a scan rate of 50 mV $s^{-1}$ using an Ag/AgCl reference electrode, following the method reported by Yanwu Zhang[80,119]

As shown in Fig. 9, the anodic current increased with higher NaOH concentrations, which is attributed to the generation of more high-potential hydroxyl radicals that facilitate glucose oxidation.[8,111] Among the tested concentrations, 0.5 M NaOH produced the highest anodic response, a trend consistent with literature findings on the critical role of alkaline media in non-enzymatic glucose sensing.[124] Therefore, selected as the optimal alkaline electrolyte for further electrochemical studies.

In All experiments were performed in alkaline solution 50 mM with and without the addition of 2 mM glucose. In the potential range −0.8 to 1 V at a scan rate of 50 mV $s^{-1}$.

The cyclic voltammograms of bare graphite, graphite/graphene, and $Fe_2O_3/CuFe_2O_4$/GNPs/Gt electrodes, recorded in the absence and presence of 2 mM glucose, are presented in Fig. 10(A–C). The bare graphite electrode exhibited a very low oxidation current for glucose, indicating limited electrocatalytic activity.[81,110]

In contrast, the graphite/GNPs-modified electrode demonstrated a notably higher oxidation current, which can be attributed to the enhanced electrical conductivity of graphene.[2,93,118] Furthermore, the $Fe_2O_3/CuFe_2O_4$/GNPs/Gt electrode showed a significant increase in the oxidation peak current, along with the appearance of a distinct shoulder peak around 0.6 V. This suggests improved electrocatalytic behavior due to the incorporation of the $Fe_2O_3/CuFe_2O_4$ nanocomposite[86,92] Additionally, the electrocatalytic oxidation of 2 mM glucose on the $Fe_2O_3/CuFe_2O_4$/GNPs/Gt modified electrode in 0.5 M NaOH was investigated across scan rates ranging from 50 to 500 mV $s^{-1}$ (Fig. 11A). The resulting linear relationship between the peak current and scan rate (see Fig. 11B) confirms that the glucose electrooxidation process is surface-controlled under these conditions.[81] Overall, the results

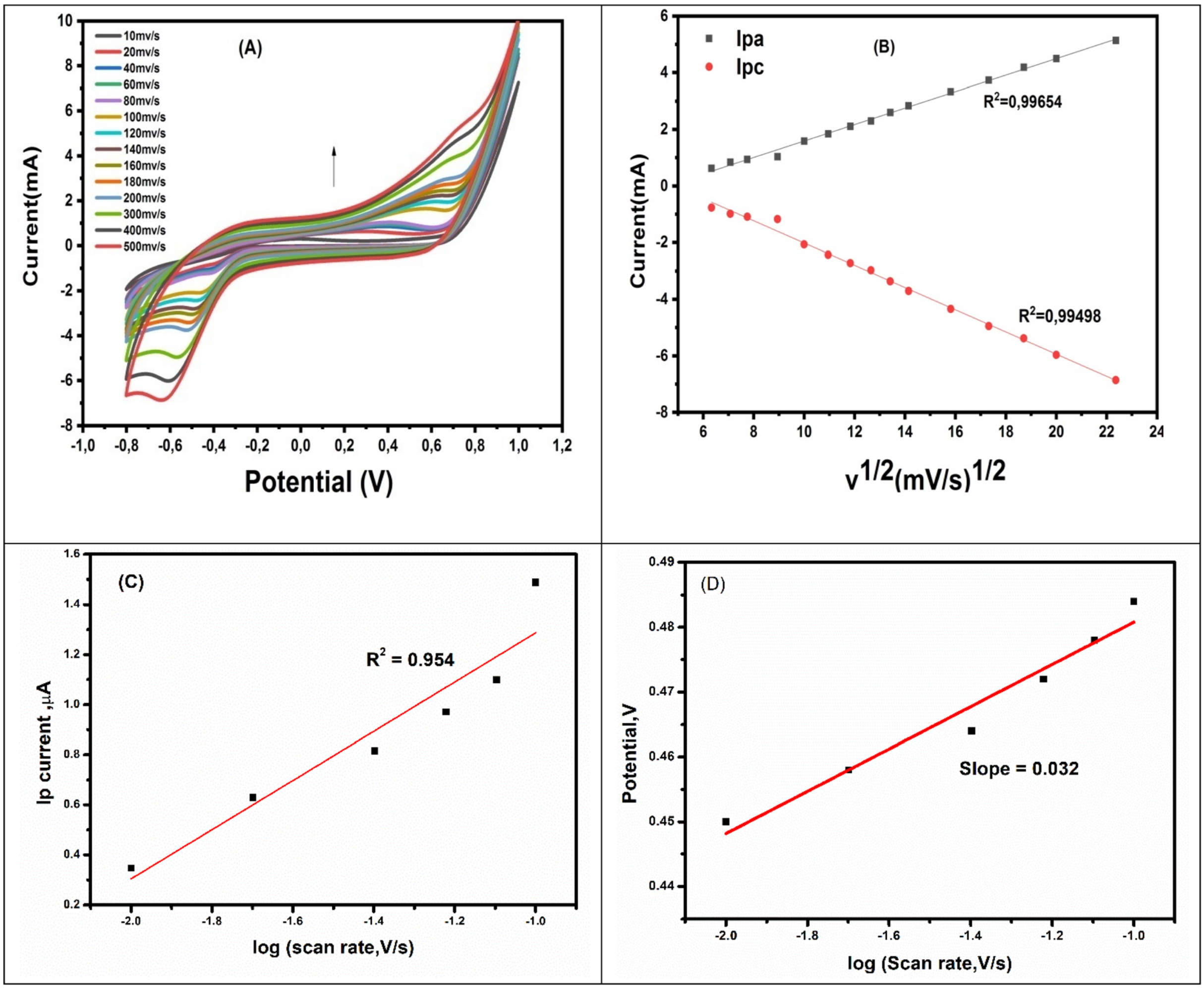

Fig. 11 (A) Cyclic voltammograms of $Fe_2O_3/CuFe_2O_4$/GNPs/Gt in 0.5 mM NaOH solution with 02 mM Glucose at different scan rates; from inner to outer: 10, 20, 40, 50, 60, 80, 100, 120, 140, 160, 180, 200, 300, 400 and 500 mV $s^{-1}$. Inset shows the plots of (B) peak current *versus* the square root of scan rate.

confirm that the presence of graphene is essential for improving the conductivity and sensitivity of the electrode, while the $Fe_2O_3/CuFe_2O_4$ nanocomposite contributes to enhanced electrocatalytic activity. The $Fe_2O_3/CuFe_2O_4$/GNPs/Gt electrode thus benefits from a synergistic effect between graphene and the metal oxide nanocomposite.[45]

**3.3.1. Electron transfer kinetics and proposed catalytic mechanism.** To gain deeper insight into the kinetics of glucose oxidation on the $Fe_2O_3/CuFe_2O_4$/GNPs/Gt nanocomposite, cyclic voltammetry (CV) was conducted at varying scan rates (10–100 mV $s^{-1}$) in 0.5 M NaOH containing 2.0 mM glucose. As shown in Fig. 11C, the anodic peak current ($I_p$) increased linearly with the log square root of the scan rate ($\nu$), indicating that the glucose oxidation process is primarily diffusion-controlled. However, the shift in peak potential with increasing scan rate suggests quasi-reversible kinetics, which are appropriately described by Laviron's equation for quasi-reversible redox systems.[54]

To further analyze the electron transfer process at the $Fe_2O_3/CuFe_2O_4$/GNPs/Gt electrode, Laviron's eqn (2) for quasi-reversible redox systems was applied:[40]

$$E_p = E_0 + RT/(1-\alpha)\,nF\ln(RTk_0/(1-\alpha)nF) + RT/(1-\alpha)nF\ln \text{v} \quad (2)$$

where $E_p$ is the peak potential (V), $\nu$ is the scan rate (V $s^{-1}$), $n$ is the number of electrons transferred, $\alpha$ is the charge transfer coefficient (assumed to be 0.5), $k_0$ is the standard rate constant, and $R$, $T$, and $F$ are universal gas constant, absolute temperature, and Faraday constant respectively. A plot of $E_p$ *versus* $\lg \nu$ (Fig. 11D) showed a linear trend with a slope of approximately 30 mV per decade. Using the slope expression from Laviron's formalism, Slope = $RT(1-\alpha)nF$, and substituting $R = 8.314$ J $mol^{-1}$ $K^{-1}$ $R = 8.314$ J $mol^{-1}$ $K^{-1}$, $T = 298$ K, $F = 96485$ C $mol^{-1}$, and the observed slope of 0.032 V, the number of electrons transferred was calculated as approximately $n \approx 2.05$.[102] This value indicates that the glucose oxidation process at the

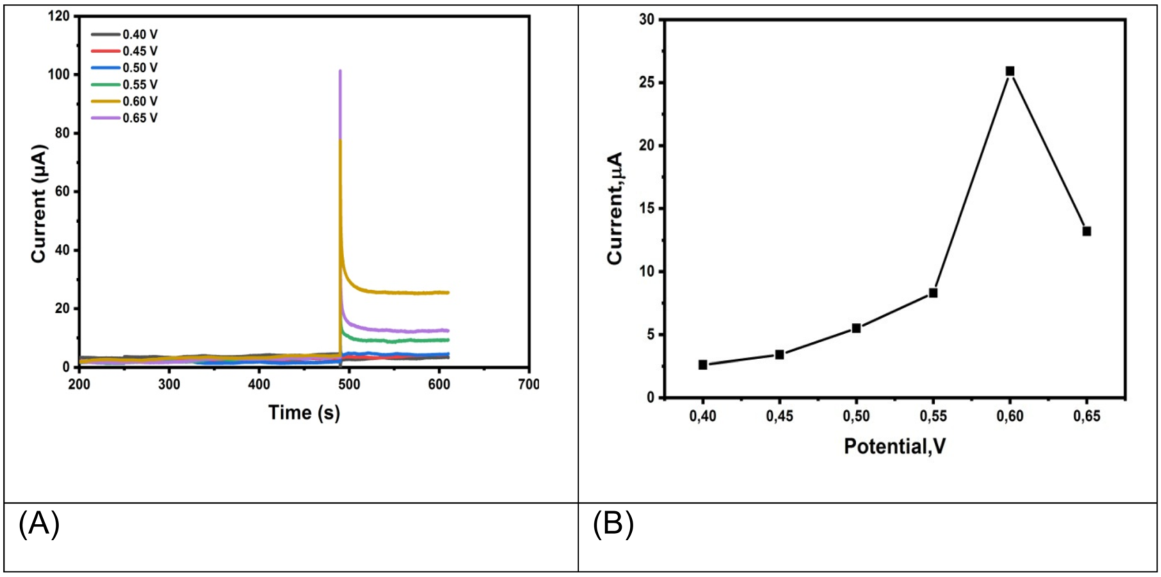

Fig. 12 (A) Chronoamperometric response and (B) the of linearity plot of the $Fe_2O_3/CuFe_2O_4$/GNPs/Gt electrode at different potentials 0.4 V, 0.45 V, 0.5 V, 0.55 V, 0.6 V and 0.65 V with a fixed addition of 10 μL glucose into gently stirred 0.5 M NaOH solution.

electrode surface involves the transfer of two electrons, consistent with the conversion of glucose to gluconolactone.[81,101]

The efficient electrocatalytic performance of the $Fe_2O_3/CuFe_2O_4$/GNPs/Gt composite electrode can be ascribed to the synergistic interaction among its redox-active constituents. Copper ions play a central catalytic role, wherein $Cu^{2+}$ is electrochemically oxidized to $Cu^{3+}$, which then chemically oxidizes glucose to gluconolactone, following an EC (Electrochemical–Chemical) mechanism:[81,102]

$$Cu^{2+} \rightarrow Cu^{3+} + e^-$$

$$Cu^{3+} + \text{glucose} \rightarrow Cu^{2+} + \text{gluconolactone}$$

This redox cycling facilitates sustained catalytic turnover and electron transfer. Additionally, iron centers from both $Fe_2O_3$ and $CuFe_2O_4$ may contribute to the redox process either through direct participation or by assisting in the regeneration of $Cu^{2+}$ species *via* internal electron shuttling.[19] The inclusion of Graphene Nanoplatelets (GNPs) further enhances performance by providing a highly conductive network that accelerates charge transport, minimizes charge transfer resistance ($R_{ct}$), and prevents nanoparticle agglomeration, thereby maximizing the exposure of active sites.[123] Collectively, these factors result in enhanced electron transfer kinetics, reduced overpotential, and a heightened anodic response during glucose oxidation. In

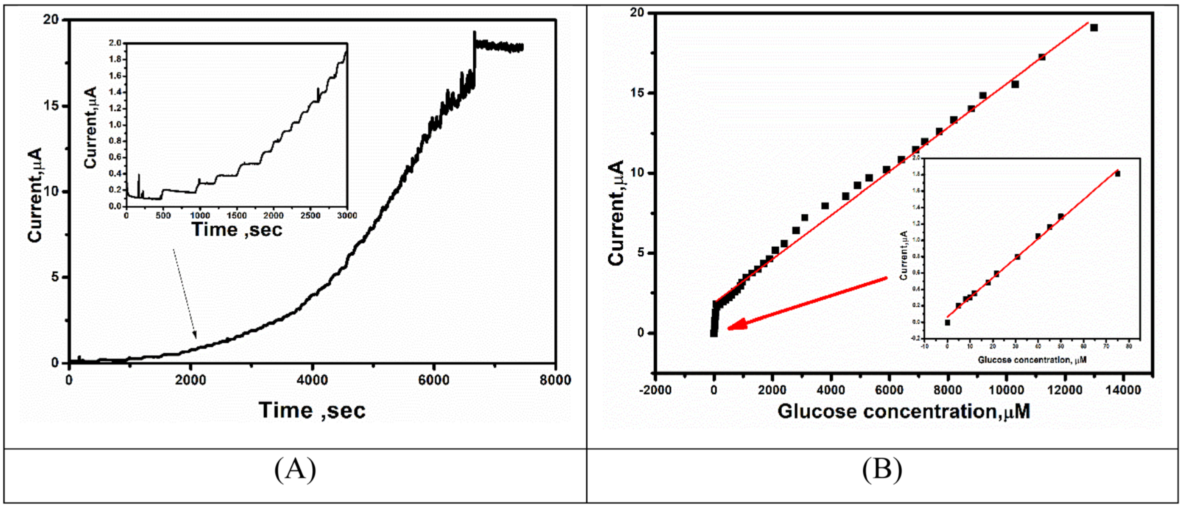

Fig. 13 (A) Chronoamperometric responses and (B) the linear relationships between the catalytic current and the concentration of $Fe_2O_3/CuFe_2O_4$/GNPs/Gt electrode upon the successive addition of glucose into gently stirred 0.5 M NaOH at 0.6 V.

Fig. 11A, a distinct shoulder peak appears at approximately 0.6 V prior to the main oxidation peak (∼0.75 V). This feature is attributed to the initial adsorption and partial dehydrogenation of glucose molecules on the $Fe_2O_3/CuFe_2O_4$/GNPs/Gt surface. In alkaline media, non-enzymatic glucose oxidation proceeds through multiple steps, beginning with the formation of a glucose-derived intermediate, such as gluconolactone or enediol species. This step is facilitated by the electrochemically generated $Cu^{3+}$ or $Fe^{3+}$ species, which act as active catalytic centers. The shoulder peak therefore corresponds to the oxidation of glucose to an intermediate, while the subsequent peak represents further oxidation to the final product. Similar multi-step oxidation behavior with shoulder peaks has been reported in literature for Cu- and Fe-based glucose sensors, confirming the complex surface-controlled reaction mechanism.[19,38]

**3.3.2. Effects of applied potential.** The applied potential significantly affects the chronoamperometric electrochemical sensor's signal response.[56] Therefore, the effect of different applied potential on the glucose response of the $Fe_2O_3/CuFe_2O_4$/GNPs/Gt modified electrode was investigated. The chronoamperometric measurements were conducted in 0.5 M NaOH by successive injections of 10 µL glucose at 120 seconds intervals, under various applied potentials ranging 0.40–0.65 V, as illustrated in Fig. 12A and B.

The current response increased progressively with rising detection potential, reaching a maximum at 0.60V.[19] However, further increasing the potential to 0.65 V resulted in a decline in current response, likely due to the non-specific oxidation of interfering species or by-products at higher potentials.[38,81] Therefore, +0.60 V was selected as the optimal detection potential for subsequent glucose sensing due to its balance between sensitivity and selectivity.

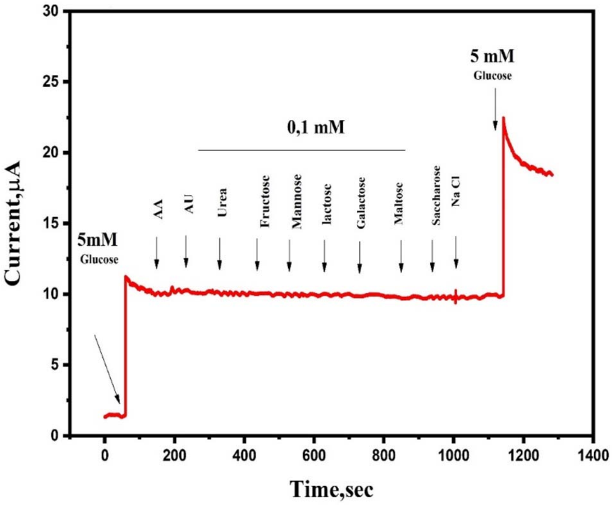

Fig. 14 Response to sequential injections of 5 mM glucose, 0.1 mM of ascorbic acid (AA), uric acid (UA), urea, fructose, mannose, lactose, galactose, maltose, saccharose, NaCl, and 5 mM glucose.

### 3.4. Calibration curve

To evaluate the sensitivity and detection limit of the non-enzymatic glucose sensor based on the $Fe_2O_3/CuFe_2O_4$/GNPs/Gt modified electrode, chronoamperometric measurements were performed under optimized conditions in 0.5 M NaOH solution.[19] Successive injections of varying glucose concentrations were introduced over a broad concentration range. The corresponding chronoamperometric responses are shown in Fig. 13A.

The resulting calibration curves (Fig. 13B) demonstrate excellent linearity and sensitivity. The sensor exhibited high

Table 2 Evaluation of the proposed glucose sensor and the others modified electrodes in the literature[a]

| Modification type of sensor | Linear range | Limit of detection (µM) | Sensitivity (µA $mM^{-1}$ $cm^{-2}$) | Ref. |
|---|---|---|---|---|
| Nickel foam electrode modified with $CuFe_2O_4$ nanotubes | 20 µM to 5 mM<br>500 µM to 25 mM | 0.22 mM, 22 µM | 1239<br>219 for $H_2O_2$ | 111 |
| Cu-Doped ZnO nanoparticles | 1 nM to 100 µM | 0.7 nM | — | 74 |
| RGOs-$Cu_2O$ nanocomposites | 0.01 to 6 mM | 0.055 µM | 185 | 121 |
| $CuFe_2O_4$/PPyCore-shell nanoparticles | 0.1–7.5 mM | 1 µM | 1824 | 93 |
| Ni/NiO/graphene | 00.299–6.44 mM | 1.8 µM | 1997 | 118 |
| Hexagonal Co $_3$O $_4$/reduced graphene oxide sheets | 0.001–0.5 mM | 0.4 µM | 1315 | 105 |
| $Co_3O_4$/CuO nanorod array supported on carbon cloth | Fast response time of 1.9 s | 0.38 µM | 405 | 20 |
| $Cu(OH)_2$/3D porous graphene foam (PGF) | 0.0012–6 mM | 1.2 µM | 3360 | 91 |
| g-$C_3N_4$/α-$Fe_2O_3$ | 0.002–2.4 mM | Not specified | — | 57 |
| $CoNi_2Se_4$/rGO | 1–4 mM | 0.65 µM | 18 890 | 3 |
| ZnO/$Co_3O_4$/reduced graphene oxide (rGO) nanocomposite | 0.015–10 mM | 0.093 µM | 1551.38 | 44 |
| NiO/$Fe_2O_3$ | 50 µM to 2.867 mM | 3.9 µM | 230.5 | 58 |
| Ni-NPs/Ppy/GRE-based | 1–1000 µM | 0.4 µM | 2873 | 29 |
| $Fe_2O_3/CuFe_2O_4$/GNPs nanocomposite | 5–75 µM<br>75–13 000 µM | 0.049 µM<br>25 µM | 624 | This work |

[a] GCE glassy carbon electrode, MWCNT multi-walled carbon nanotubes $CuFe_2O_4$ copper ferrite,rGO reduced graphene oxide nanocomposite, Au gold nanoparticles, PPy core–shell nanoparticle polypyrrole core–shell nanoparticle, GRE graphite rod electrode.

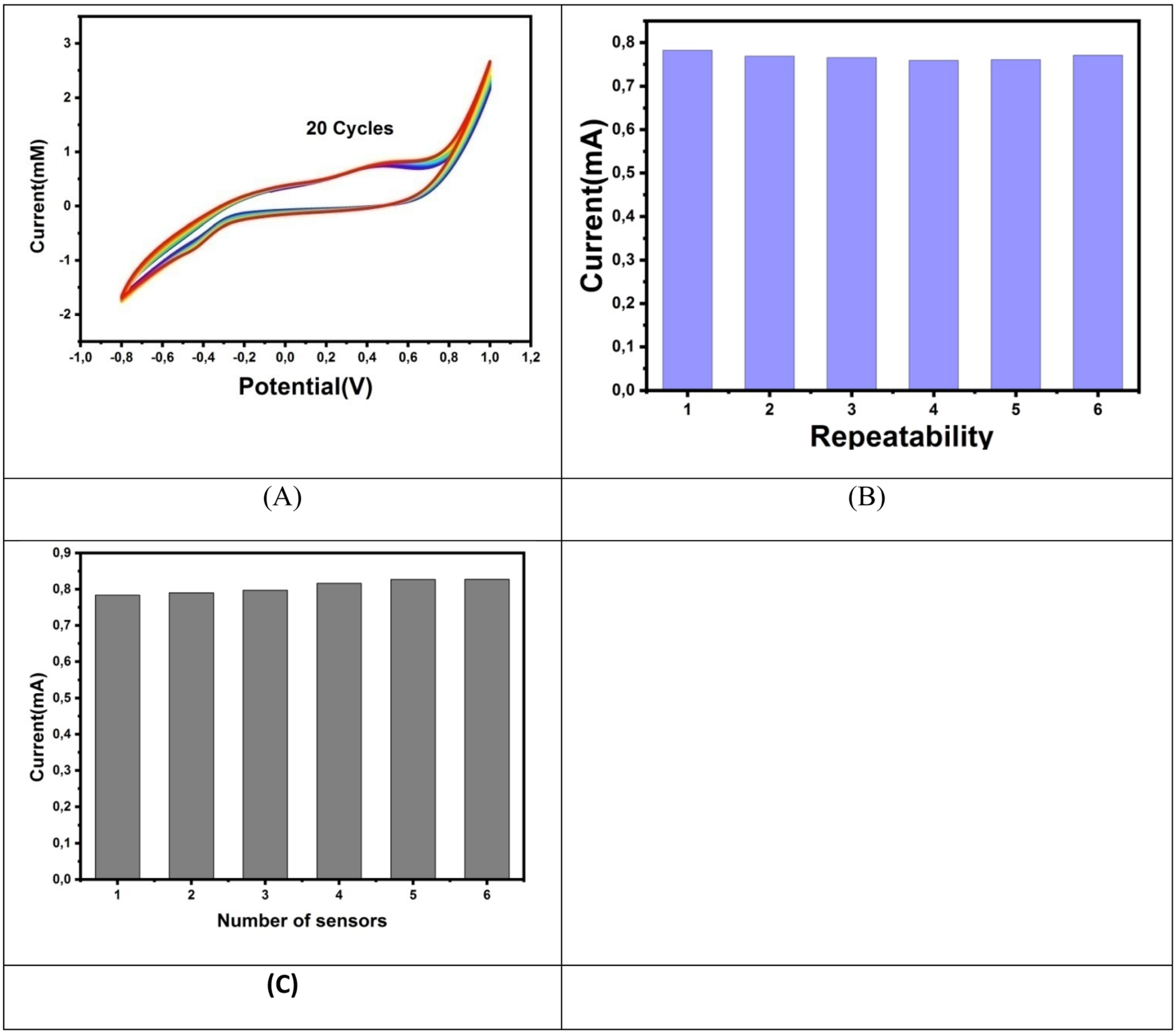

(A)

(B)

**(C)**

Fig. 15 (a) CV curves of graphite/$Fe_3O_4$/$CuFe_2O_4$/GNPs/Gt in 2 mM glucose at NaOH 0.5 M for 20 cycles. (b) Repeatability of the voltammetric responses of 2 mM glucose in NaOH 0.5 M (repeatability $n = 6$). (c) reproducibility ($n = 6$ sensors).

Table 3 Validation of the $Fe_2O_3$/$CuFe_2O_4$/GNPs/Gt sensor against a standard commercial glucose meter

| Glucose concentration mM | | | |
|---|---|---|---|
| The proposed sensor | The commercial instrument | RSD (%) | Recovery (%) |
| 2.26 | 2.31 | 2.42 | 97.83 |
| 4.84 | 4.82 | 0.92 | 100.41 |
| 7.74 | 7.64 | 1.38 | 101.31 |
| 9.36 | 9.49 | 2.96 | 98.63 |

sensitivities of 0.062 $\mu A\ \mu M^{-1}\ cm^{-2}$ and 0.001329 $\mu A\ \mu M^{-1}\ cm^{-2}$ within the respective concentration ranges.[81] The proposed sensor reveals two distinct linear response ranges: from 5.0 to 75 μM and from 75 to 1000 μM μM with $R^2 = 0.9983$. The limit of detection (LOD) was calculated using the IUPAC-recommended formula LOD $= 3\sigma/S$, where $\sigma$ is the standard deviation of the blank ($n = 7$) and $S$ is the slope of the calibration curve. The resulting LOD was 0.049 μM, indicating very high analytical sensitivity under laboratory conditions. It is important to note, however, that this value reflects performance in buffered standard solutions and may differ in complex biological matrices due to sample interference or electrode fouling. Comparatively, recent reports on non-enzymatic glucose sensors have achieved LODs in the range of 0.055–10 μM. Our result is among the lowest reported, which we attribute to the synergistic conductivity and catalytic activity of the $Fe_2O_3$/$CuFe_2O_4$/GNPs/Gt nanocomposite.

Moreover, the rapid and consistent responses—observed for the modified sensor every 120 seconds following each glucose addition—highlight the strong electrocatalytic synergy provided by the nanocomposite materials.

A comparison with previously reported electrochemical glucose sensors is provided in Table 2. Notably, the current system demonstrates superior sensitivity relative to many other non-enzymatic detection approaches.

### 3.5. Selectivity

To evaluate the real-world applicability of the sensor, selectivity tests were repeated using clinically relevant concentrations: 5 mM glucose and 0.1 mM interferents (AA, UA, urea, fructose, mannose, lactose, galactose,maltose, and sucrose).[33,43] As shown in the updated Fig. 14, the sensor response to glucose remained dominant, while the signal change due to interferents was negligible (<5%), confirming excellent selectivity in a physiologically relevant matrix. Additionally, NaCl was included not as an electroactive interferent but to simulate physiological ionic strength, as its presence can influence the electrochemical environment.[123] The stable current response in the presence of NaCl further confirms the robustness of the electrode under biological conditions.[44,80]

### 3.6. Stability, repeatability, and reproducibility

The stability of the non-enzymatic $Fe_2O_3/CuFe_2O_4$/GNPs/Gt sensor was evaluated *via* cyclic voltammetry in 0.5 M NaOH containing 2 mM glucose over 20 continuous cycles. As shown in Fig. 15a, the oxidation current in the 20th cycle retained 86.87% of its initial value, indicating good electrochemical stability during repeated use.[81] To assess repeatability,[38] the same electrode was tested six consecutive times under identical conditions (Fig. 15b), yielding a relative standard deviation (RSD) of 1.09%, which demonstrates excellent short-term consistency.[122] Reproducibility was further examined using six independently fabricated electrodes tested with 2 mM glucose under the same conditions (Fig. 15c). The resulting RSD was 2.36%, confirming the reliability[44] and consistency of the sensor fabrication process.

### 3.7. Real sample examination

The evaluation of human serum samples using the newly developed non-enzymatic glucose sensor is summarized in Table 3. The relative standard deviation (RSD) values ranged from 0.92% to 2.96%, with an average of 1.92%, indicating strong measurement precision and reproducibility.[107] These results closely matched those obtained from a commercial glucose biosensor used in a local hospital, demonstrating that the sensor's performance is not limited to standard glucose solutions. Instead, it is reliably applicable to real human serum samples, confirming its potential for practical clinical use. Similar studies have also reported high precision and accurate detection of glucose in human serum using non-enzymatic sensors based on metal oxide/graphene composites: Haghparas[114] *et al.* demonstrated effective detection with RSD values below 3% in human serum samples using CuO/ZnO hollow microstructures,[38,114] and Hussein, B,[44] *et al.* confirmed good recovery and stability in serum and practical real sample analysis using $ZnO/Co_3O_4$/rGO/GCE.

## 4. Conclusion

In this study, a simple synthesized methods for $Fe_2O_3/CuFe_2O_4$ nanocomposite was evaluated. Then, a novel non-enzymatic glucose sensor based on a $Fe_2O_3/CuFe_2O_4$/GNPs nanocomposite-modified electrode was successfully developed and characterized. The optimized composition (graphene : graphite ratio of 45 : 55 with 10% $Fe_2O_3/CuFe_2O_4$) demonstrated excellent electrocatalytic activity, high conductivity, and enhanced electron transfer kinetics, as confirmed by cyclic voltammetry and electrochemical impedance spectroscopy. The sensor exhibited high sensitivity, a low detection limit, and a wide linear range for glucose detection under optimal conditions in 0.5 M NaOH.The electrode showed outstanding stability, repeatability, and reproducibility, with minimal signal loss over repeated use and consistent performance across multiple fabricated sensors. Selectivity tests confirmed the sensor's ability to distinguish glucose in the presence of common interfering species. Furthermore, the sensor demonstrated strong agreement with commercial glucose biosensors in the analysis of real human serum samples, highlighting its potential for clinical and point-of-care applications. Overall, the developed sensor offers a promising, low-cost, and reliable platform for non-enzymatic glucose detection, with practical applicability in biomedical diagnostics and glucose monitoring.

## Conflicts of interest

The authors declare that there is no conflict of interest.

## Data availability

The authors confirm that the data supporting the findings of this study are available within the article.

## References

1 K. Ali, B. Ali, A. Jabbar, S. Iqbal, I. Ahmad and M. I. Bashir, Synthesis, Structural, Dielectric and Magnetic Properties of Cufe2o4/Mno2 Nanocomposites, *J. Magn. Magn. Mater.*, 2017, **434**, 30–36.

2 A. Ambrosi, C. K. Chua, A. Bonanni and M. Pumera, Electrochemistry of Graphene and Related Materials, *Chem. Rev.*, 2014, **114**, 7150–7188.

3 B. G. Amin, J. Masud and M. Nath, A Non-Enzymatic Glucose Sensor Based on a Coni 2 Se 4/Rgo Nanocomposite with Ultrahigh Sensitivity at Low Working Potential, *J. Mater. Chem. B*, 2019, **7**, 2338–2348.

4 A. Ali, K. Karim, O. Hakami, W. M. Alamier, S. K. Ali, T. Zelai, M. S. Rashid, A. K. Tareen and E. A. Al-Harthi, Recent Progress in Metal Oxide-Based Electrode Materials for Safe and Sustainable Variants of Supercapacitors, *Front. Chem.*, 2024, **12**, 1402563.

5 K. Atacan, Cufe2o4/Reduced Graphene Oxide Nanocomposite Decorated with Gold Nanoparticles as a New Electrochemical Sensor Material for L-Cysteine Detection, *J. Alloys Compd.*, 2019, **791**, 391–401.

6 A. Aykaç, H. Gergeroglu, B. Beşli, E. Ö. Akkaş, A. Yavaş, S. Güler, F. Güneş and M. Erol, An Overview on Recent Progress of Metal Oxide/Graphene/Cnts-Based Nanobiosensors, *Nanoscale Res. Lett.*, 2021, **16**, 65.

7 A. Aykaç, and İ. Ok, Graphene/Metal Oxide-Based Nanocomposite for Electrochemical Sensors, in *Optical Properties of Metal Oxide Nanostructures*, Springer, 2023, pp. 331–70.

8 T. G. Satheesh Babu and T. Ramachandran, Development of Highly Sensitive Non-Enzymatic Sensor for the Selective Determination of Glucose and Fabrication of a Working Model, *Electrochim. Acta*, 2010, **55**, 1612–1618.

9 A. Bagheri, A. Fallah, J. Karczewski, A. Eslami, A. M. S. Asadi and G. Boczkaj, Investigating Covid-19 Active Pharmaceutical Ingredients (Apis) Degradation Using Peroxydisulfate/Femnox Binary Metal Oxide/Ultrasound System, *Water Resour. Ind.*, 2024, **31**, 100232.

10 G. Balkourani, T. Damartzis, A. Brouzgou and P. Tsiakaras, Cost Effective Synthesis of Graphene Nanomaterials for Non-Enzymatic Electrochemical Sensors for Glucose: A Comprehensive Review, *Sensors*, 2022, **22**, 355.

11 A. J. Bard, L. R. Faulkner, and H. S. White, *Electrochemical Methods: Fundamentals and Applications*, John Wiley & Sons, 2022.

12 G. Beamson, High Relution Xps of Organic Polymers. The Scienta Esca 300 Database, *ICIplc*, 1993, **5**, 10.

13 S. Berciaud, S. Ryu, L. E. Brus and T. F. Heinz, Probing the Intrinsic Properties of Exfoliated Graphene: Raman Spectroscopy of Free-Standing Monolayers, *Nano Lett.*, 2009, **9**, 346–352.

14 M. C. Biesinger, Advanced Analysis of Copper X-Ray Photoelectron Spectra, *Surf. Interface Anal.*, 2017, **49**, 1325–1334.

15 M. C. Biesinger, B. P. Payne, A. P. Grosvenor, L. W. M. Lau, A. R. Gerson and R. St C. Smart, Resolving Surface Chemical States in Xps Analysis of First Row Transition Metals, Oxides and Hydroxides: Cr, Mn, Fe, Co and Ni, *Appl. Surf. Sci.*, 2011, **257**, 2717–2730.

16 D. A. C. Brownson and C. E. Banks, Graphene Electrochemistry: An Overview of Potential Applications, *Analyst*, 2010, **135**, 2768–2778.

17 D. A. C. Brownson, C. W. Foster and C. E. Banks, The Electrochemical Performance of Graphene Modified Electrodes: An Analytical Perspective, *Analyst*, 2012, **137**, 1815–1823.

18 R. A. Sobh and H. S. Magar, Innovative formulation of a functional nano-copolymer derived from glycidyl methacrylate and acrylonitrile as an exceptionally sensitive and selective electrochemical sensor for folic acid detection in pharmaceutical and food samples, *Nanoscale*, 2025, **17**, 18359–18376.

19 S. Carinelli, P. A. Salazar-Carballo, J. E. Rosa Melián and F. García-García, Porous Copper Oxide Thin Film Electrodes for Non-Enzymatic Glucose Detection, *Chemosensors*, 2023, **11**, 260.

20 S. Cheng, S. DelaCruz, C. Chen, Z. Tang, T. Shi, C. Carraro and R. Maboudian, Hierarchical Co3o4/Cuo Nanorod Array Supported on Carbon Cloth for Highly Sensitive Non-Enzymatic Glucose Biosensing, *Sens. Actuators, B*, 2019, **298**, 126860.

21 R. M. Cornell, and U. Schwertmann, *The Iron Oxides: Structure, Properties, Reactions, Occurrences and Uses*, John Wiley & Sons, 2003.

22 E. Cuara, U. Sierra, A. Mercado, E. D. Barriga-Castro, A. Cortés, C. Gallardo-Vega, M. Valle-Orta and S. Fernández, Synthesis of Copper Oxides-Graphene Composites for Glucose Sensing, *Carbon Trends*, 2021, **4**, 100050.

23 B. D. Cullity, and S. R. Stock, *Elements of X-Ray Diffraction, Prentice Hall*, Upper Saddle River, NJ, 2001, p. 388.

24 Q. Dong, H. Ryu and Y. Lei, Metal Oxide Based Non-Enzymatic Electrochemical Sensors for Glucose Detection, *Electrochim. Acta*, 2021, **370**, 137744.

25 D. R. Dreyer, S. Park, C. W. Bielawski and R. S. Ruoff, The Chemistry of Graphene Oxide, *Chem. Soc. Rev.*, 2010, **39**, 228–240.

26 R. F. Egerton, *Physical Principles of Electron Microscopy*, Springer, 2016.

27 G. A. El-Fatah, H. S. Magar, R. Y. A. Hassan, R. Mahmoud, A. A. Farghali and M. E. M. Hassouna, A Novel Gallium Oxide Nanoparticles-Based Sensor for the Simultaneous Electrochemical Detection of Pb2+, Cd2+ and Hg2+ Ions in Real Water Samples, *Sci. Rep.*, 2022, **12**, 20181.

28 A. M. El-Kosasy, M. H. A. Rahman and S. H. Abdelaal, Graphene Nanoplatelets in Potentiometry: A Nanocomposite Carbon Paste and Pvc Based Membrane Sensors for Analysis of Vilazodone Hcl in Plasma and Milk Samples, *Talanta*, 2019, **193**, 9–14.

29 G. Emir, Y. Dilgin, A. Ramanaviciene and A. Ramanavicius, Amperometric Nonenzymatic Glucose Biosensor Based on Graphite Rod Electrode Modified by Ni-Nanoparticle/Polypyrrole Composite, *Microchem. J.*, 2021, **161**, 105751.

30 A. C. Ferrari, F. Bonaccorso, V. Fal'Ko, K. S. Novoselov, S. Roche, P. Bøggild, S. Borini, F. H. L. Koppens, V. Palermo and N. Pugno, Science and Technology Roadmap for Graphene, Related Two-Dimensional Crystals, and Hybrid Systems, *Nanoscale*, 2015, **7**, 4598–4810.

31 F. Foroughi, M. Rahsepar, M. J. Hadianfard and H. Kim, Facile Synthesis and Electrochemical Performance of Graphene-Modified Cu2o Nanocomposite for Use in Enzyme-Free Glucose Biosensor, *Iran. J. Chem. Chem. Eng.*, 2020, **39**, 1–10.

32 A. García-Miranda Ferrari, C. W. Foster, P. J. Kelly, D. A. C. Brownson and C. E. Banks, Determination of the Electrochemical Area of Screen-Printed Electrochemical Sensing Platforms, *Biosensors*, 2018, **8**, 53.

33 R. Ghosh, L. Xiao and M. Z. Yates, Nonenzymatic Glucose Sensor Using Bimetallic Catalysts, *ACS Appl. Mater. Interfaces*, 2023, **16**, 17–29.

34 J. I. Goldstein, D. E. Newbury, J. R. Michael, N. W. M. Ritchie, J. H. J. Scott, and D. C. Joy, *Scanning Electron Microscopy and X-Ray Microanalysis*, Springer, 2017.

35 J. M. Gonçalves, L. V. de Faria, A. B. Nascimento, R. L. Germscheidt, S. Patra, L. P. Hernández-Saravia, J. A. Bonacin, R. A. A. Munoz and L. Angnes, Sensing Performances of Spinel Ferrites Mfe2o4 (M= Mg, Ni, Co, Mn, Cu and Zn) Based Electrochemical Sensors: A Review, *Anal. Chim. Acta*, 2022, **1233**, 340362.

36 M. Gotić and S. Musić, Mössbauer, Ft-Ir and Fe Sem Investigation of Iron Oxides Precipitated from Feso4 Solutions, *J. Mol. Struct.*, 2007, **834**, 445–453.

37 A. P. Grosvenor, B. A. Kobe, M. C. Biesinger and N. S. McIntyre, Investigation of Multiplet Splitting of Fe 2p Xps Spectra and Bonding in Iron Compounds, *Surf. Interface Anal.*, 2004, **36**, 1564–1574.

38 Z. Haghparas, Z. Kordrostami, M. Sorouri, M. Rajabzadeh and R. Khalifeh, Highly Sensitive Non-Enzymatic Electrochemical Glucose Sensor Based on Dumbbell-Shaped Double-Shelled Hollow Nanoporous Cuo/Zno Microstructures, *Sci. Rep.*, 2021, **11**, 344.

39 M. S. Hashem and H. S. Magar, Creative Synthesis of Ph-Dependent Nanoporous Pectic Acid Grafted with Acrylamide and Acrylic Acid Copolymer as an Ultrasensitive and Selective Riboflavin Electrochemical Sensor in Real Samples, *Int. J. Biol. Macromol.*, 2024, **280**, 136022.

40 A. Heller and B. Feldman, Electrochemical Glucose Sensors and Their Applications in Diabetes Management, *Chem. Rev.*, 2008, **108**, 2482–2505.

41 D. Hernández-Ramírez, L. H. Mendoza-Huizar, C. A. Galán-Vidal, G. Y. Aguilar-Lira and G. A. Álvarez-Romero, Development of a Non-Enzymatic Glucose Sensor Based on Fe2o3 Nanoparticles-Carbon Paste Electrodes, *J. Electrochem. Soc.*, 2022, **169**, 067507.

42 Z. Hsine, R. Mlika, N. Jaffrezic-Renault and H. Korri-Youssoufi, Review—Recent Progress in Graphene Based Modified Electrodes for Electrochemical Detection of Dopamine, *Chemosensors*, 2022, **10**, 249.

43 Yu-W. Hsu, T.-K. Hsu, C.-L. Sun, Y.-T. Nien, N.-W. Pu and M.-D. Ger, Synthesis of Cuo/Graphene Nanocomposites for Nonenzymatic Electrochemical Glucose Biosensor Applications, *Electrochim. Acta*, 2012, **82**, 152–157.

44 B. A. Hussein, A. A. Tsegaye, G. Shifera and A. M. Taddesse, A Sensitive Non-Enzymatic Electrochemical Glucose Sensor Based on a Zno/Co 3 O 4/Reduced Graphene Oxide Nanocomposite, *Sens. Diagn.*, 2023, **2**, 347–360.

45 H. Jeong, L. Ku Kwac, C. G. Hong and H. G. Kim, Direct Growth of Flower Like-Structured Cufe Oxide on Graphene Supported Nickel Foam as an Effective Sensor for Glucose Determination, *Mater. Sci. Eng., C*, 2021, **118**, 111510.

46 D. Jiang, Q. Liu, K. Wang, J. Qian, X. Dong, Z. Yang, X. Du and B. Qiu, Enhanced Non-Enzymatic Glucose Sensing Based on Copper Nanoparticles Decorated Nitrogen-Doped Graphene, *Biosens. Bioelectron.*, 2014, **54**, 273–278.

47 L. Jothi, N. Jayakumar, S. K. Jaganathan and G. Nageswaran, Ultrasensitive and Selective Non-Enzymatic Electrochemical Glucose Sensor Based on Hybrid Material of Graphene Nanosheets/Graphene Nanoribbons/Nickel Nanoparticle, *Mater. Res. Bull.*, 2018, **98**, 300–307.

48 L. Kabir, Y. J. Joo, K. Y. Cho and W.-C. Oh, Electrochemical Approach for Nonenzymatic Glucose Sensing with Noble Metal-Free 2d Graphene-Based Ternary Nanocomposite, *Sens. Actuators, A*, 2024, **372**, 115367.

49 P. K. Kalambate, N. Larpant, R. P. Kalambate, W. Niamsi, V. Primpray, C. Karuwan and W. Laiwattanapaisal, A Portable Smartphone-Compatible Ratiometric Electrochemical Sensor with Ultrahigh Sensitivity for Anticancer Drug Mitoxantrone Sensing, *Sens. Actuators, B*, 2023, **378**, 133103.

50 P. V. Kamat, Graphene-Based Nanoarchitectures. Anchoring Semiconductor and Metal Nanoparticles on a Two-Dimensional Carbon Support, *J. Phys. Chem. Lett.*, 2010, **1**, 520–527.

51 A. Kaniyoor and S. Ramaprabhu, A Raman Spectroscopic Investigation of Graphite Oxide Derived Graphene, *AIP Adv.*, 2012, **2**, 032183.

52 A. Kumar, P. Choudhary, A. Kumar, H. C. C. Pedro and V. Krishnan, Recent Advances in Plasmonic Photocatalysis Based on Tio2 and Noble Metal Nanoparticles for Energy Conversion, Environmental Remediation, and Organic Synthesis, *Small*, 2022, **18**, 2101638.

53 A. Lasia, Electrochemical Impedance Spectroscopy and Its Applications, in *Modern Aspects of Electrochemistry*, Springer, 2002, pp. 143–248.

54 E. J. J. Laviron, General Expression of the Linear Potential Sweep Voltammogram in the Case of Diffusionless Electrochemical Systems, *J. Electroanal. Chem. Interfacial Electrochem.*, 1979, **101**, 19–28.

55 R. Li, X. Deng and L. Xia, Non-Enzymatic Sensor for Determination of Glucose Based on Ptni Nanoparticles Decorated Graphene, *Sci. Rep.*, 2020, **10**, 16788.

56 J. Liu, J. Shen, S. Ji, Q. Zhang and W. Zhao, Research Progress of Electrode Materials for Non-Enzymatic Glucose Electrochemical Sensors, *Sens. Diagn.*, 2023, **2**, 36–45.

57 L. Liu, J. Wang, C. Wang and G. Wang, Facile Synthesis of Graphitic Carbon Nitride/Nanostructured Α-Fe2o3 Composites and Their Excellent Electrochemical Performance for Supercapacitor and Enzyme-Free Glucose Detection Applications, *Appl. Surf. Sci.*, 2016, **390**, 303–310.

58 L. Luo, J. Cui, Y. Wang, Y. Wang, H. Zheng, Y. Qin, X. Shu, D. Yu, Y. Zhang and Y. Wu, Synthesis of Nio/Fe2o3 Nanocomposites as Substrate for the Construction of Electrochemical Biosensors, *J. Solid State Electrochem.*, 2018, **22**, 1763–1770.

59 R. Lv, E. Cruz-Silva and M. Terrones, Building Complex Hybrid Carbon Architectures by Covalent Interconnections: Graphene–Nanotube Hybrids and More, *ACS Nano*, 2014, **8**, 4061–4069.

60 M. E. G. Lyons and M. P. Brandon, The Oxygen Evolution Reaction on Passive Oxide Covered Transition Metal Electrodes in Aqueous Alkaline Solution. Part 1-Nickel, *Int. J. Electrochem. Sci.*, 2008, **3**, 1386–1424.

61 H. S. Magar, H. Abdelghany, M. N. Abbas, U. Bilitewski and R. Y. A. Hassan, Fast Analysis of Staphylococcus Aureus in Food Products Using Disposable Label-Free Nano-Electrochemical Immunosensor Chips, *Microchem. J.*, 2023, **193**, 109097.

62 H. S. Magar, P. K. Brahman and R. Y. A. Hassan, Disposable Impedimetric Nano-Immunochips for the Early and Rapid Diagnosis of Vitamin-D Deficiency, *Biosens. Bioelectron.:X*, 2022, **10**, 100124.

63 H. S. Magar, E. S. M. Duraia and R. Y. A. Hassan, Dopamine Fast Determination in Pharmaceutical Products Using Disposable Printed Electrodes Modified with Bimetal Oxides Carbon Nanotubes Nanocomposite, *Sci. Rep.*, 2025, **15**, 11229.

64 H. S. Magar, A. M. El Nahrawy, R. Y. A. Hassan and A. B. Abou Hammad, Nanohexagonal Iron Barium Titanate Nanoparticles Surface-Modified Nife2o4 Composite Screen-Printed Electrode for Enzymatic Glucose Monitoring, *RSC Adv.*, 2024, **14**, 34948–34963.

65 H. S. Magar and A. M. Fahim, Sensing Platform Based on Rgo/Cellulose-Triazole Composite for the Electrochemical Detection of Mercury (Ii) Ions in Food Samples, *Microchem. J.*, 2025, **215**, 114243.

66 H. S. Magar, A. M. Fahim and M. S. Hashem, Accurate, Affordable, and Easy Electrochemical Detection of Ascorbic Acid in Fresh Fruit Juices and Pharmaceutical Samples Using an Electroactive Gelatin Sulfonamide, *RSC Adv.*, 2024, **14**, 39820–39832.

67 H. S. Magar, M. Fayez, F. Febbraio and R. Y. A. Hassan, Esterase-2 Mutant-Based Nanostructured Amperometric Biosensors for the Selective Determination of Paraoxon (Neurotoxin), *Anal. Biochem.*, 2025, **698**, 115751.

68 H. S. Magar, M. S. Hashem and R. A. Sobh, Design of Metal Oxide Nanoparticles-Embedded Polymeric Nanocomposites for Hydrogen Peroxide Chronoamperometric Sensor, *Polym. Compos.*, 2024, **45**, 3653–3665.

69 H. S. Magar, R. Y. A. Hassan and M. N. Abbas, Non-Enzymatic Disposable Electrochemical Sensors Based on Cuo/Co3o4@Mwcnts Nanocomposite Modified Screen-Printed Electrode for the Direct Determination of Urea, *Sci. Rep.*, 2023, **13**, 2034.

70 H. S. Magar, B. A. Hemdan, H. R. M. Rashdan and R. Y. A. Hassan, Rapid and Selective Detection of Foodborne Pathogens Using a Disposable Bio-Sensing System Designed by Stepwise Antibody Immobilization on Aunps@Cu-Mof Nanocomposite, *J. Anal. Test.*, 2024, **8**, 478–492.

71 H. S. Magar, E. E. A. E. Magd, R. Y. A. Hassan and A. M. Fahim, Rapid Impedimetric Detection of Cadmium Ions Using Nanocellulose/Ligand/Nanocomposite (Cnt/Co3o4), *Microchem. J.*, 2022, **182**, 107885.

72 H. M. Mahdy, Y. M. Abbas, H. S. Magar, R. Y. A. Hassan and E. S. M. Duraia, Silver Vanadate and Cerium Oxide Decorated Graphene Oxide Ternary Heterostructure Nanocomposites: Structural, Electrochemical, and Optoelectrical Properties, *J. Mater. Sci.: Mater. Electron.*, 2024, **35**, 1891.

73 A. R. Mahfouz, H. G. Nada, H. S. Magar, K. Z. ElBaghdady and R. Y. A. Hassan, Nano-Biosensors for Rapid Detection of Antibiotic Resistance Genes Blactx-M in Escherichia Coli and Blakpc in *Klebsiella Pneumoniae*, *Int. J. Biol. Macromol.*, 2025, **310**, 143216.

74 A. Mahmoud, M. Echabaane, O. Karim, J. Boudon, L. Saviot, N. Millot and R. Ben Chaabane, Cu-Doped Zno Nanoparticles for Non-Enzymatic Glucose Sensing, *Molecules*, 2021, **26**, 929.

75 L. M. Malard, M. Assunção Pimenta, G. Dresselhaus and M. S. Dresselhaus, Raman Spectroscopy in Graphene, *Phys. Rep.*, 2009, **473**, 51–87.

76 S. Mallesh, G. Minji and Ki H. Kim, Cubic to Tetragonal Phase Transition in Cufe2o4 Nanoparticles, *J. Magn.*, 2021, **26**, 7.

77 A. M. Mansour, H. S. Magar, A. Elzwawy, A. B. Abou Hammad and A. M. El Nahrawy, Structural, Optical, and Electrochemical Properties of Tungsten-Doped Cadmium Zinc Phosphate Nanoporous Materials for Energy Storage and Peroxide Detection, *RSC Adv.*, 2025, **15**, 15670–15693.

78 A. James Marsden, D. G. Papageorgiou, C. Valles, A. Liscio, V. Palermo, M. A. Bissett, R. J. Young and I. A. Kinloch, Electrical Percolation in Graphene–Polymer Composites, *2D Materials*, 2018, **5**, 032003.

79 M. Mbebou, S. Polat and H. Zengin, Sustainable Cauliflower-Patterned Cufe2o4 Electrode Production from Chalcopyrite for Supercapacitor Applications, *Nanomaterials*, 2023, **13**, 1105.

80 A. Mohammadpour-Haratbar, S. Mohammadpour-Haratbar, Y. Zare, K. Y. Rhee and S.-J. Park, A Review on Non-Enzymatic Electrochemical Biosensors of Glucose Using Carbon Nanofiber Nanocomposites, *Biosensors*, 2022, **12**, 1004.

81 G. A. Naikoo, H. Salim, I. U. Hassan, T. Awan, F. Arshad, M. Z. Pedram, W. Ahmed and A. Qurashi, Recent Advances in Non-Enzymatic Glucose Sensors Based on Metal and Metal Oxide Nanostructures for Diabetes Management-a Review, *Front. Chem.*, 2021, **9**, 748957.

82 K. Nakamoto, *Infrared and Raman Spectra of Inorganic and Coordination Compounds, Part B: Applications in Coordination, Organometallic, and Bioinorganic Chemistry*, John Wiley & Sons, 2009.

83 X. Nan, Y. Zhang, J. Shen, R. Liang, J. Wang, L. Jia, X. Yang, W. Yu and Z. Zhang, A Review of the Establishment of Effective Conductive Pathways of Conductive Polymer Composites and Advances in Electromagnetic Shielding, *Polymers*, 2024, **16**, 2539.

84 A. V. Naumkin, A. Kraut-Vass, S. W. Gaarenstroom, and C. J. Powell, Nist X-Ray Photoelectron Spectroscopy Database, *Nist Standard Reference Database 20, Version 4.1*, US Department of Commerce, Washington, 10 (2012), p. T4T88K.

85 J. Navarro-Laboulais, J. J. García-Jareño, J. Agrisuelas and F. Vicente, Eis Behavior of Polyethylene + Graphite

Composite Considered as an Approximation to an Ensemble of Microelectrodes, *J. Compos. Sci.*, 2024, **8**, 378.

86 D. Neravathu, A. R. Paloly and M. J. Bushiri, Hybrid Nanomaterial of Znfe2o4/Α-Fe2o3 Implanted Graphene for Electrochemical Glucose Sensing Application, *Diamond Relat. Mater.*, 2020, **106**, 107852.

87 P. Pazhamalai, V. Krishnan, M. S. M. Saleem, S.-J. Kim and H.-W. Seo, Investigating Composite Electrode Materials of Metal Oxides for Advanced Energy Storage Applications, *Nano Convergence*, 2024, **11**, 30.

88 S. M. Ramteke, M. Walczak, M. De Stefano, A. Ruggiero, A. Rosenkranz and M. Marian, 2d Materials for Tribo-Corrosion and-Oxidation Protection: A Review, *Adv. Colloid Interface Sci.*, 2024, **331**, 103243.

89 S. Rodsud and W. Limbut, A Simple Electrochemical Sensor Based on Graphene Nanoplatelets Modified Glassy Carbon Electrode (Grnps/Gce) for Highly Sensitive Detection of Yohimbine (Yoh), *J. Electrochem. Soc.*, 2019, **166**, B771.

90 S. S. Selima, M. Khairy and M. A. Mousa, Comparative Studies on the Impact of Synthesis Methods on Structural, Optical, Magnetic and Catalytic Properties of Cufe2o4, *Ceram. Int.*, 2019, **45**, 6535–6540.

91 I. Shackery, U. Patil, A. Pezeshki, N. M. Shinde, S. Kang, S. Im and S. Chan Jun, Copper Hydroxide Nanorods Decorated Porous Graphene Foam Electrodes for Non-Enzymatic Glucose Sensing, *Electrochim. Acta*, 2016, **191**, 954–961.

92 Z. Shaghaghi, A. Saghebi Shalghuni and S. Jafari, Fe2o3/Cuo Hybrid Nanostructures as Electrode Materials for Glucose Detection, *Anal. Bioanal. Chem. Res.*, 2024, **11**, 343–360.

93 Z. Shahnavaz, P. M. Woi and Y. Alias, A Hydrothermally Prepared Reduced Graphene Oxide-Supported Copper Ferrite Hybrid for Glucose Sensing, *Ceram. Int.*, 2015, **41**, 12710–12716.

94 M. S. Hashem and H. S. Magar, Inventive pectic acid grafted with polyacrylamide for a highly sensitive and selective non-enzymatic dopamine sensor in pharmaceutical samples, *RSC Adv.*, 2025, **15**, 33758–33772.

95 M. D. P. Silva, F. C. Silva, F. S. M. Sinfrônio, A. R. Paschoal, E. N. Silva and C. W. A. Paschoal, The Effect of Cobalt Substitution in Crystal Structure and Vibrational Modes of Cufe2o4 Powders Obtained by Polymeric Precursor Method, *J. Alloys Compd.*, 2014, **584**, 573–580.

96 A. J. Slate, D. A. C. Brownson, S. A. D. Ahmed, G. C. Smith, K. A. Whitehead and C. E. Banks, Exploring the Electrochemical Performance of Graphite and Graphene Paste Electrodes Composed of Varying Lateral Flake Sizes, *Phys. Chem. Chem. Phys.*, 2018, **20**, 20010–20022.

97 G. Socrates, *Infrared and Raman Characteristic Group Frequencies: Tables and Charts*, John Wiley & Sons, 2004.

98 S. Stankovich, D. A. Dikin, G. H. B. Dommett, K. M. Kohlhaas, E. J. Zimney, E. A. Stach, R. D. Piner, S. T. Nguyen and R. S. Ruoff, Graphene-Based Composite Materials, *Nature*, 2006, **442**, 282.

99 D. Stauffer, and A. Aharony, *Introduction to Percolation Theory*, Taylor & Francis, 2018.

100 I. Švancara, K. Vytřas, K. Kalcher, A. Walcarius and J. Wang, Carbon Paste Electrodes in Facts, Numbers, and Notes: A Review on the Occasion of the 50-Years Jubilee of Carbon Paste in Electrochemistry and Electroanalysis, *Electroanalysis*, 2009, **21**, 7–28.

101 Y. Tian, Q. Wang, J. Niu, J. Liang, Y. Geng, X. Liu, J. Wang and M. Ma, Cuco-Based Carbonate Hydrosulfide Nanoarray Supported on Carbon Cloth as Electrocatalysts for Glucose Sensing, *ACS Appl. Nano Mater.*, 2024, **7**, 25249–25258.

102 K. E. Toghill and R. G. Compton, Metal Nanoparticle Modified Boron Doped Diamond Electrodes for Use in Electroanalysis, *Electroanalysis*, 2010, **22**, 1947–1956.

103 M. G. Trachioti, A. Ch Lazanas and M. I. Prodromidis, Shedding Light on the Calculation of Electrode Electroactive Area and Heterogeneous Electron Transfer Rate Constants at Graphite Screen-Printed Electrodes, *Microchim. Acta*, 2023, **190**, 251.

104 T. U. Tran Thi, Van H. Phan, H. T. P. Nguyen, T. L. Nguyen, An N. Vu and K. Le Tien, Synthesis of Magnetic Cufe2o4/Fe2o3 Core-Shell Materials and Their Application in Photo-Fenton-Like Process with Oxalic Acid as a Radical-Producing Source, *Asian Ceram. Soc.*, 2021, **9**, 1091–1102.

105 A. T. E. Vilian, B. Dinesh, M. Rethinasabapathy, S.-K. Hwang, C.-S. Jin, Y. S. Huh and Y.-K. Han, Hexagonal Co 3 O 4 Anchored Reduced Graphene Oxide Sheets for High-Performance Supercapacitors and Non-Enzymatic Glucose Sensing, *J. Mater. Chem. A*, 2018, **6**, 14367–14379.

106 M. Wang, M. Wang, T. Shen, M. Wang, D. Zhang, Z. Tong and J. Chen, One-Pot Synthesis of Α-Fe2o3 Nanoparticles-Decorated Reduced Graphene Oxide for Efficient Nonenzymatic H2o2 Biosensor, *Sens. Actuators, B*, 2014, **190**, 645–650.

107 M. Wang, M. Shi, E. Meng, F. Gong and F. Li, Non-Enzymatic Glucose Sensor Based on Three-Dimensional Hierarchical Co3o4 Nanobooks, *Micro Nano Lett.*, 2020, **15**, 191–195.

108 M. Wei, Y. Qiao, H. Zhao, J. Liang, T. Li, Y. Luo, S. Lu, X. Shi, W. Lu and X. Sun, Electrochemical Non-Enzymatic Glucose Sensors: Recent Progress and Perspectives, *Chem. Commun.*, 2020, **56**, 14553–14569.

109 J.-B. Wu, M.-L. Lin, X. Cong, He-N. Liu and P.-H. Tan, Raman Spectroscopy of Graphene-Based Materials and Its Applications in Related Devices, *Chem. Soc. Rev.*, 2018, **47**, 1822–1873.

110 P. Wu, Q. Shao, Y. Hu, J. Jin, Y. Yin, H. Zhang and C. Cai, Direct Electrochemistry of Glucose Oxidase Assembled on Graphene and Application to Glucose Detection, *Electrochim. Acta*, 2010, **55**, 8606–8614.

111 H. Xia, J. Li, L. Ma, Q. Liu and J. Wang, Electrospun Porous Cufe2o4 Nanotubes on Nickel Foam for Nonenzymatic Voltammetric Determination of Glucose and Hydrogen Peroxide, *J. Alloys Compd.*, 2018, **739**, 764–770.

112 K. Xu and W. Zheng, Fabrication of Graphene-Based Ammonia Sensors: A Review, *Curr. Nanosci.*, 2024, **20**, 578–598.

113 T. Yamashita and P. Hayes, Analysis of Xps Spectra of Fe2+ and Fe3+ Ions in Oxide Materials, *Appl. Surf. Sci.*, 2008, **254**, 2441–2449.

114 D. Yang, Y. Chen, S. Che and K. Wang, Recent Advances in Non-Enzymatic Glucose Sensors Based on Nanomaterials, *Coatings*, 2025, **15**, 892.

115 J. Yu, X. Shan, D. Zhou, X. Zhao and W. Sheng, Non-Enzymatic Glucose Detection by Fe2o3 Nanorods-Reduced Graphene under Physiological Ph, *Curr. Pharm. Anal.*, 2024, **20**, 275–282.

116 B. Zhang, Y. Yang, Y. Liu, Z.-D. Huang, Y.-B. He and J.-K. Kim, Percolation Threshold of Graphene Nanosheets as Conductive Additives in Li 4 Ti 5 O 12 Anodes of Li-Ion Batteries, *Nanoscale*, 2013, **5**, 2100–2106.

117 L. Zhang, F. Zhang, X. Yang, G. K. Long, Y. P. Wu, T. F. Zhang, K. Leng, Y. Huang, Y. F. Ma and A. Yu, Porous 3d Graphene-Based Bulk Materials with Exceptional High Surface Area and Excellent Conductivity for Supercapacitors, *Sci. Rep.*, 2013, **3**, 1408.

118 X. Zhang, Z. Zhang, Q. Liao, S. Liu, Z. Kang and Y. Zhang, Nonenzymatic Glucose Sensor Based on *in Situ* Reduction of Ni/Nio-Graphene Nanocomposite, *Sensors*, 2016, **16**, 1791.

119 Y. Zhang, E. Zhou, Y. Li and X. He, A Novel Nonenzymatic Glucose Sensor Based on Magnetic Copper Ferrite Immobilized on Multiwalled Carbon Nanotubes, *Anal. Methods*, 2015, **7**, 2360–2366.

120 X. Zhao, D. Chu, X. Zhang, C. Gao, Y. He and W. Bai, Growth and Characterization of Carbon Nanotubes and Study of Modified Carbon Fiber—a Review, *Diamond Relat. Mater.*, 2024, **147**, 111308.

121 D.-L. Zhou, J.-J. Feng, L.-Y. Cai, Q.-X. Fang, J.-R. Chen and A.-J. Wang, Facile Synthesis of Monodisperse Porous Cu2o Nanospheres on Reduced Graphene Oxide for Non-Enzymatic Amperometric Glucose Sensing, *Electrochim. Acta*, 2014, **115**, 103–108.

122 C. Zhu, G. Yang, H. Li, D. Du and Y. Lin, Electrochemical Sensors and Biosensors Based on Nanomaterials and Nanostructures, *Anal. Chem.*, 2015, **87**, 230–249.

123 H. Zhu, F. Shi, M. Peng, Y. Zhang, S. Long, R. Liu, J. Li and Z. Yang, Non-Enzymatic Electrochemical Glucose Sensors Based on Metal Oxides and Sulfides: Recent Progress and Perspectives, *Chemosensors*, 2025, **13**, 19.

124 H. Zhu, L. Li, W. Zhou, Z. Shao and X. Chen, Advances in Non-Enzymatic Glucose Sensors Based on Metal Oxides, *J. Mater. Chem. B*, 2016, **4**, 7333–7349.

125 Y. Zhu, S. Murali, W. Cai, X. Li, Ji W. Suk, J. R. Potts and R. S. Ruoff, Graphene and Graphene Oxide: Synthesis, Properties, and Applications, *Adv. Mater.*, 2010, **22**, 3906–3924.

126 A. Zoppi, C. Lofrumento, E. M. Castellucci and Ph Sciau, Al-for-Fe Substitution in Hematite: The Effect of Low Al Concentrations in the Raman Spectrum of Fe2o3, *J. Raman Spectrosc.*, 2008, **39**, 40–46.